Constitution of the binary M-Sb systems (M = Ti, Zr, Hf) and physical properties of MSb$_2$

A. Tavassoli[a,b], A. Grytsiv[a,c,d,*], F. Failamani[a], G. Rogl[a,c,d], S. Puchegger[b], H. Müller[c], P. Broz[e,f], F. Zelenka[e,f], D. Macciò[g], A. Saccone[g], G. Giester[h], E. Bauer[c,d], M. Zehetbauer[b], P. Rogl[a,d]

[a] Institute of Materials Chemistry and Research, University of Vienna, Währingerstr., 42, A-1090 Wien, Austria
[b] Faculty of Physics, University of Vienna, Boltzmanngasse 5, A-1090 Wien, Austria
[c] Institute of Solid State Physics, TU Wien, Wiedner Hauptstr., 8-10, A-1040 Wien, Austria
[d] Christian Doppler Laboratory for Thermoelectricity, Wien, Austria
[e] Masaryk University, Faculty of Science, Department of Chemistry, Kotlarska 2, 611 37 Brno, Czech Republic
[f] Masaryk University, Central European Institute of Technology, CEITEC MU, Kamenice 753/5, Brno 625 00, Czech Republic
[g] Dipartimento di Chimica e Chimica Industriale, Universita di Genova, Via Dodecaneso 31, I-16146 Genova, Italy
[h] Institute of Mineralogy and Crystallography, University of Vienna, Althanstraße 14, A-1090 Wien, Austria

A B S T R A C T

This study is closely related to the chemical interactions in thermoelectric joints of a hot metal electrode with p- and n-type skutterudite. As a result of this work, a first and complete phase diagram has been constructed for the Ti—Sb system as well as partial phase diagrams (> 65 at.% Sb) for the systems Zr—Sb and Hf—Sb. Investigations are based on X-ray powder and single crystal analyses (determination of the crystal structure of Ti$_5$Sb$_8$ with Zr$_{2.6}$Ti$_{2.4}$Sb$_8$-type, space group $I4_1 22$; R$_F$ = 0.032), electron probe microanalyses (EPMA) and differential thermal analyses (DTA). Physical properties were evaluated for the binary compounds MSb$_2$ (M = Ti, Zr, Hf) comprising electrical resistivity (from 4.2 K to 825 K), specific heat, thermal conductivity and thermal expansion coefficient (from 4.2 K to 300 K), Seebeck coefficient (from 300 K to 825 K) and elastic moduli at 300 K.

These data will serve to evaluate the potential of MSb$_2$ compounds (M = Ti, Zr, Hf) for thermoelectric devices, where these phases predominantly appear in the diffusion zones of the hot metal electrode with p- and n-type skutterudite.

1. Introduction

In the last years titanium antimonides have been subjected to intensive investigation in several fields such as electrode materials for lithium batteries, hydrogen storage materials as well as interface materials for skutterudite-based thermoelectric (TE) devices. Besides being tribo-pyrophoric, the antimonides of group IV elements have the ability to intercalate lithium atoms in their structures, and can be used as materials for negative electrodes [1–3]. Furthermore, titanium antimonides Ti$_3$Sb and Ti$_2$Sb absorb considerable amounts of hydrogen where the cubic host lattice of Ti$_3$Sb retains the Cr$_3$Si (A15) type structure after hydrogen absorption [4–6] whilst tetragonal Ti$_2$Sb changes to an 'undistorted' La$_2$Sb-type with square-planar Ti layers (space group $I4/mmm$) [6]. Moreover, antimony based skutterudites are known for their high thermoelectric performance and are regarded as promising materials for thermoelectric power generation working in the intermediate temperature region [7–9]. For device fabrication not

only a high thermoelectric efficiency of the p- and n-legs is essential, but also good electric and thermal contact materials are required, i.e. particularly the hot electrodes should have good transport and mechanical properties compatible with the p- and n-legs. Unlike bismuth telluride-based TE devices, tin soldering is not favorable for joining skutterudite-based materials with the electrodes because of the low melting point of tin solders. CoSb$_3$ based skutterudites were successfully joined to Mo, Mo$_{50}$Cu$_{50}$ and W$_{80}$Cu$_{20}$ electrodes using a titanium interlayer [10–12], and inspection of the diffusion zones shows the formation of TiSb and TiSb$_2$ phases. The evanescence of such diffusion layers on the p- and n-type skutterudites in contact with group IV metals is shown in Fig. 1 for the cases of Ti and Hf.

Thus the afore mentioned interest concerning the various group IV metal antimonides in the bonding diffusion layers documents the urgent need for detailed information on phase equilibria and crystal structure of the phases in the binary M-Sb systems. In addition a particular demand concerns data on mechanical and transport properties
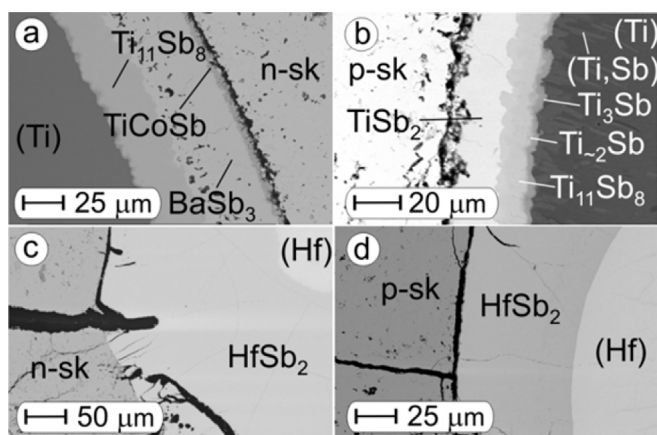
Fig. 1. Diffusion zones formed by Ti (a,b) and Hf (c,d) with n-type skutterudite $Ba_{0.3}Co_4Sb_{12}$ (a,c) and p-type skutterudite $MM_{0.75}Fe_3CoSb_{12}$ (b,d). MM stands for mischmetal (La,Ce,Pr,Nd).

for $TiSb_2$, $ZrSb_2$ and $HfSb_2$ considering their potential for the production of skutterudite based TE modules/devices.

Only for $TiSb_2$ physical properties have been studied rather extensively by Armbrüster and co-workers [13–15]. Temperature dependent electrical resistivity and Hall effect measurements for the temperature range from 4.2 K to 300 K were carried out on a single crystal in different crystallographic directions. The compound was characterized by X-ray single crystal (SC) diffraction, Raman spectroscopy, X-ray absorption spectroscopy and L_3-edge spectrometry. The same group also performed a detailed investigation on the homogeneity region by X-ray powder diffraction (XPD), differential scanning calorimetry (DSC), energy- and wavelength-dispersive X-ray (EDX and WDX) analyses. A narrow homogeneity range was reported for $TiSb_2$ at 700 °C extending from $Ti_{33.1(1)}Sb_{66.9}$ to $Ti_{33.3(2)}Sb_{66.7}$. This compound was furthermore found to melt incongruently at about 1000 °C with a liquidus temperature at 1080 °C. Atom bonding was discussed on the basis of calculations of band structure, density of states (DOS) and electron localization function (ELF).

Our detailed literature survey revealed no information so far on the physical properties of MSb_2 (M = Ti, Zr, Hf) compounds (such as thermal conductivity, specific heat, thermal expansion coefficients at low temperature and mechanical properties). The only data found for $ZrSb_2$ are those of E. Garcia and J.D. Corbett [16] concerning the electrical resistivity in the temperature range from 4.2 K to 300 K, and the statement of F. Hulliger [17] that $ZrSb_2$ and $HfSb_2$ show metallic conduction and a small p-type thermo-power.

It should be noted that in contrast to $TiSb_2$ (space group *I4/mcm*, $CuAl_2$ structure type [18], Table 1), the low temperature modifications of {Zr, Hf}Sb_2 crystallize in the $TiAs_2$-type structure (space group *Pnnm*). It needs to be mentioned here that the so-called high temperature modification β-$ZrSb_2$, described as Sb-deficient $ZrSb_{2-x}$ (x ~ 0.04, isotypic with $PbCl_2$) [16,19], was later found to be stabilized by silicon [20], although, the amount of silicon in this compound ($ZrSb_{2-x}Si_x$) is rather low: $0.066 \le x \le 0.115$. An isotypic hafnium compound ($HfSb_{2-x}Si_x$) does not exist, but a high temperature form, β-$HfSb_2$, earlier described as UAs_2 type-structure [21], was later determined to be Hf_5Sb_9 [22] with a $a = a_0 \times \sqrt{5}$ superstructure and to exist at temperatures above 1020 °C.

Although preliminary information on the phase equilibria and crystal structure of binary phases in the Ti−Sb system exist, these data, however, are rather contradictory. The first study of this system was performed by Nowotny et al. [18,23,24] who prepared the alloys in alumina crucibles and investigated them by X-ray powder diffraction and light optical microscopy (LOM). The authors reported the formation of four intermediate compounds Ti_4Sb ($Ti_3(Ti_{0.2}Sb_{0.8})$), $Ti_{2.5}Sb$ ($Ti_2(Ti_{0.15}Sb_{0.85})$), TiSb and $TiSb_2$ (Table 1) and indicated the existence

of a eutectic between TiSb and a Ti-richer phase (probably Ti_4Sb) [18]. Employing several preparation techniques (arc-melting, melting in alumina crucibles and in silica tubes) Kjekshus et al. [25] found four titanium antimonides: Ti_3Sb (cubic β-W-type ≡ Cr_3Si-type and tetragonal Ti_3Sb-type ≡ ordering variant of W_5Si_3-type [31]), two compounds with orthorhombic structures $Ti_{1.7}Sb$ (presumable space groups *Pmma, Pmc2₁* or *Pma2*) and $Ti_{1.2}Sb$ (*Pbam* or *Pba2*). The authors, however, did neither confirm the existence of Ti_4Sb nor of $Ti_{2.5}Sb$ as reported earlier by Nowotny and coworkers [18,23,24]. As cubic Ti_3Sb was described to irreversibly transform into the tetragonal modification, the latter was considered to be a silicon and aluminium stabilized phase [26,27]. "$Ti_{1.7}Sb$" [25] was verified as Ti_5Sb_3 with the β-Yb_5Sb_3 type structure [28–30].

A critical assessment of the Ti−Sb system by J.L. Murray [31] included all eight binary phases (Ti_4Sb, Ti_3Sb (cubic and tetragonal), $Ti_{2.5}Sb$, Ti_5Sb_3, Ti_6Sb_5 ($Ti_{1.2}Sb$), TiSb and $TiSb_2$) known at that time: the schematic phase diagram Ti−Sb presented [32,33], is shown in Fig. 2a. The melting temperature was defined only for the $TiSb_2$ based phase on the result of L.D. Dudkin and V.I. Vaidanich [34] who reported a peritectic reaction ℓ + TiSb ↔ $TiSb_2$ at 1010 °C with a liquidus temperature of 1030 °C (DTA).

Since that time additional knowledge was collected on the crystal structure of the known and new phases in the systems. Based on X-ray single crystal data, Bobev and Kleinke [35], defined for the compound $Ti_{11-x}Sb_{8-y}$ the composition $Ti_{10.84}Sb_{7.74}$ (41.66 at % Sb) and the $Cr_{11}Ge_8$ type structure (lattice parameters and symmetry of this compound seem to be related to $Ti_{1.2}Sb$ (Ti_6Sb_5) [25]) (see Table 1). The determination of the crystal structure of the ternary compounds (M,Ti)$_5Sb_8$ (M = Zr, Hf, Nb, Mo) and density of states (DOS) calculations triggered interest in a "parent" isotypic binary Ti_5Sb_8 [36], which finally was found to be stable in the temperature range between 900 and 1100 °C [37]. The lattice parameters of this compound were first reported by Bie et al. [38], based on a single-crystal X-ray study (a = 0.6492(4) nm and c = 2.6514(15) nm), however, no structural details (atom coordinates and site preference) were given. X-ray single crystal- and neutron powder diffraction experiments by Derakhshan et al. [39] revealed the formation of another new ternary antimonide, Ti_2Sb, which crystallizes in a distorted La_2Sb structure (see Table 1). Kaiser et al. [40] synthesized several ternary compounds Ti_5MSb_3 (M = transition metal) with filled Mn_5Si_3 type structure (Ti_5Ga_4-type) and reported the existence of a "self-filled" binary phase $Ti_{4.80}Sb_{3.29}$ based on refinements from X-ray powder diffraction data. Binary Ti_5Sb_3 with the β-Yb_5Sb_3 type was confirmed, however, refinement of the X-ray single crystal diffraction data resulted in a nonstoichiometric composition $Ti_5Sb_{2.851(6)}$.

Our analysis of the literature data (summarized in Table 1) shows that there are at least 7 stable compounds in the binary system, however, data on phase equilibria are still very limited and require a detailed investigation of this phase diagram.

Considering all the missing data, the following tasks were defined as goals of our investigation: (i) re-investigation of the phase equilibria and crystal structure of the phases in the Ti−Sb system for the whole composition range; (ii) investigation of the melting behavior for $ZrSb_2$ and $HfSb_2$; (iii) preparation of single phase samples MSb_2 (M = Ti, Zr, Hf) for detailed investigations of (iv) physical properties such as electrical resistivity (4.2 K–825 K), thermal resistivity and specific heat (4.2–300 K), Seebeck coefficient (300–825 K), (v) determination of the elastic moduli at 300 K; and (vi) measurements of thermal expansion coefficients in the temperature range of 4.2–300 K. All the data obtained will then be discussed in comparison with available experimental values reported in the literature, and thus will ensure that a first and complete phase diagram can be constructed for the Ti−Sb system and partial phase diagrams (> 65 at.% Sb) can be derived for the systems Zr−Sb and Hf−Sb. Furthermore, this investigation is closely related to the chemical interactions in thermoelectric joints of a hot metal electrode with p- and n-type skutterudite and thereby continues our

Table 1

Crystallographic data of unary and binary phases pertinent to the system Ti−Sb.

Phase, Temperature range, °C	Space group Prototype	Lattice parameters [nm]			Comments
		a	b	c	
α-Ti, rt ≤882 °C	$P6_3/mmc$ Mg	0.29506		0.46853	[32]
β-Ti, ht 882-1670 °C	Im-$3m$ W	0.33065		–	[32]
Sb ≤630.75 °C	R-$3m$ As	0.43319		1.13742	[33]
Ti$_4$Sb[a]	$P6_3/mmc$ Mg$_3$Cu	0.5958 0.5541(4) 0.558		0.4808 0.4272(6) 0.425	[18,23] Ti$_3$(Ti$_{0.2}$Sb$_{0.8}$) XPD [6] [67], metastable impurity stabilized [25]
Ti$_3$Sb[a] Ti$_3$Sb ≤1375 °C [tw][b]	$I4/mcm$ Ti$_3$Sb (W$_5$Si$_3$ variant) Pm-$3n$ Cr$_3$Si "β-W"	1.0465 0.52187 0.52184 0.5217 0.5220(5) 0.5225(5) 0.52134–0.5228 0.5216 0.5214 0.52172(2) 0.52173(1)		0.52639	[25] XPD, SC, R$_F$ = 0.116 impurity stabilized [25] Ti rich [25] Sb rich [68] [69] T$_C$ = 6.5 K [69] T$_C$ = 5.3 K [4,70,71] [5,67] [3] XPD at 21.9 at. % Sb [tw][b] at 24.4 at. % Sb [tw][b]
Ti$_{2.5}$Sb[a]	$P4_2/mmc$ Ti$_2$Bi	0.401 0.3998(1) 0.40283(3)		1.453 1.456(5) 1.48833(5)	[24] Ti$_2$(Ti$_{0.15}$Sb$_{0.85}$) XPD, SC [72] [73] XPD impurity stabilized [25]
Ti$_2$Sb ≤1422 °C [tw][b]	$I4/mmm$ Ti$_2$Sb (dist. La$_2$Sb)	0.39546(8) 0.395684(8) 0.39371(4)	 –	1.4611(3) 1.45669(6) 1.4638(6)	[39] at 150 K, SC, R$_F$ = 0.025 [6] [tw][b]
Ti$_5$Sb$_3$ > 1600 °C [tw][b]	$Pnma$ β-Yb$_5$Sb$_3$	1.0172 1.022 1.02173(5) 1.0212(2) 1.0169(9) 1.02173(5) 1.0093(3)	0.8348 0.8354(8) 0.83281(5) 0.8308(2) 0.8342(2) 0.83281(5) 0.8250(5)	0.7135 0.7181(8) 0.71459(4) 0.7117(1) 0.7146(1) 0.71459(4) 0.71991(2)	[25] Ti$_{1.7}$Sb, SC, XPD [30] [28,29], SC, R$_F$ = 0.088 [40] Ti$_5$Sb$_{2.851(6)}$ SC, R$_F$ = 0.038 [3] XPD [74] XPD [tw][b]
Ti$_{5-x}$Sb$_{4-y}$[a]	$P6_3/mcm$ Ti$_5$Ga$_4$	0.7962(1) 0.7982(1)		0.5515(1) 0.5515(1)	[40] for Ti$_{4.80}$Sb$_{3.29}$, XPD SC, R$_F$ = 0.011
Ti$_{11-x}$Sb$_{8-y}$ ≤1328 °C [tw][b]	$Pnma$ Cr$_{11}$Ge$_8$ $Pbam$ or $Pba2$	1.46228(9) 1.486(4) 1.4654(8) 1.455	0.55972(4) 0.5572(9) 0.55777(8) 1.634	1.7644(1) 1.764(4) 1.770(2) 0.531	[35] for Ti$_{10.84}$Sb$_{7.74}$, SC, R$_F$ = 0.027 [3] XPD at 37.7 at % Sb [tw][b] [25] Ti$_{1.2}$Sb(Ti$_6$Sb$_5$), XPD
TiSb ≤1252 °C [tw][b]	$P6_3/mmc$ NiAs	0.407 0.4115 0.406 0.41033(5) 0.40158(4)		0.6309 0.6264 0.630 0.62836(8) 0.6267(1)	[18], XPD [25], XPD [70] [75] [tw][b]
Ti$_5$Sb$_8$ 900-1100 °C [37] 950-1092 °C [tw][b]	$I4_122$ Zr$_{2.6}$Ti$_{2.4}$Sb$_8$	– 0.6492(4) 0.647593(9)		– 2.6514(15) 2.64256(4)	[36,37] [38] SC [tw][b] SC, R$_F$ = 0.032
TiSb$_2$ ≤1010 °C [34] ≤1000 °C [13] ≤1051 °C [tw][b]	$I4/mcm$ CuAl$_2$	0.66531(5) 0.6666 0.6654(3) 0.66528(2) 0.66539(3) 0.66544(3) 0.6656(2) 0.66495(6) 0.66572(8)	 – –	0.58092(7) 0.5817 0.5806(3) 0.58071(3) 0.58084(4) 0.58082(5) 0.5813(1) 0.58063(5) 0.5809(1)	[76], XPD [18], XPD [77], XPD [13,14] XSC, R$_F$ = 0.013 [13,15] XPD, Ti$_{33.3(2)}$Sb$_{66.7}$, Ti rich [13,15] XPD, Ti$_{33.1(1)}$Sb$_{66.9}$, Sb rich [1] XPD Ti rich [tw][b] Sb rich [tw][b]

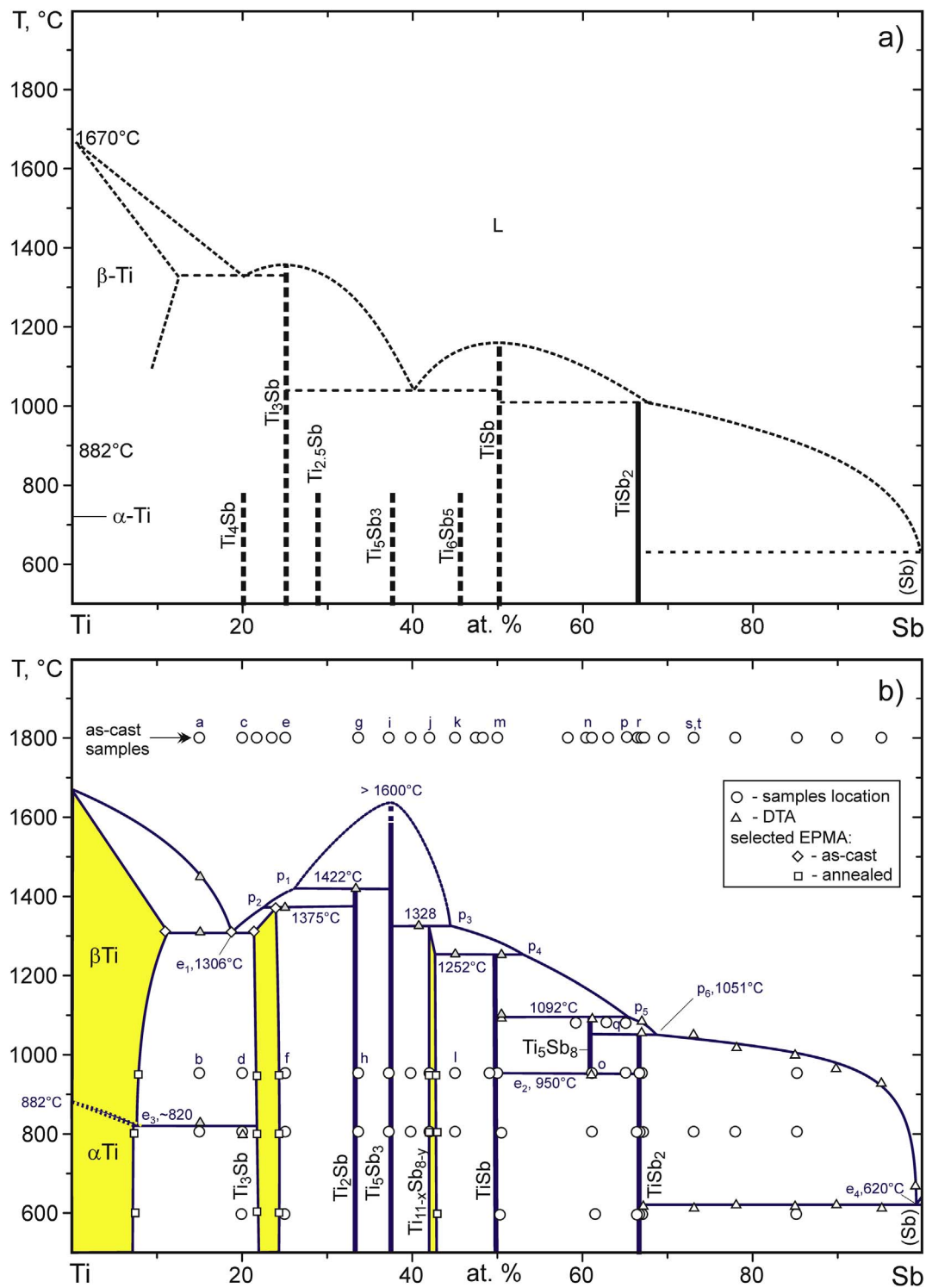[a] The phase is not observed in current investigation.

[b] [tw] - this work.

Fig. 2. Phase diagram Ti−Sb after [31] (a) and constructed in current work (b). Codes from "a" to "t" correspond to the respective SEM images on Fig. 3.

systematic studies on binary Sb containing systems such as published for {V,Nb,Ta}−Sb [41].

2. Experimental details

Alloys of about 1.5 g each were prepared by conventional arc-melting on a water-cooled copper hearth under Ti-gettered inert gas atmosphere (argon, 5N) from elements with purity above 99.9 wt%. For the composition range up to 60 at.% Sb, ingots of Ti and Sb were used, whilst for samples with higher antimony content pre-compacts of Ti and

Sb powders were applied. ZrSb$_2$ and HfSb$_2$, were prepared from arc-melted Zr$_3$Sb and Hf$_3$Sb master alloys that were powdered and compacted with antimony powder, cold pressed prior to final arc-melting. In order to compensate the weight losses of antimony during arc-melting or reaction about 3 wt% Sb were added. Repeated flipping over and re-melting homogenized the reguli. The samples were placed in alumina crucibles, sealed under vacuum in quartz ampoules and heat treated at 600 °C (20–60 days), 800 °C (10–30 days) and 950 °C (6–20 days). In some cases specimens were also prepared by isothermal reactions of the compacted powders at 800 °C and 950 °C. Single crystals

of Ti_5Sb_8 were obtained from the sample $Ti_{35}Sb_{65}$ heated in an alumina crucible at 1080 °C for 2 days followed by quenching in water.

Large samples (~0.75 cm^3) for the measurement of physical properties, were prepared from powders of Ti (≤75 μm), Zr (≤200 μm), Hf (≤75 μm) and Sb (≤150 μm) cold pressed and sintered in evacuated silica tubes at 800 °C for 6–8 days. The specimens obtained were hand crushed into powders (grain size below 75 μm) in a glove box (H_2O and O_2 content ≤ 5 ppm) and subsequently hot-pressed in a graphite die with 10 mm diameter under 56 MPa employing a uniaxial hot press (HP, type: W 200/250-2200-200-KS from FCT, Germany) using 5N Ar as inert atmosphere at a temperature of 850 °C.

The phase structures of the samples were investigated by X-ray powder diffraction (XPD) collected from a HUBER-Guinier image plate with monochromatic Cu-K$_{\alpha 1}$ radiation (λ = 0.154056 nm) and pure Ge (99.9999%) as internal standard. Precise lattice parameters were calculated by least squares fits to the indexed 2θ values (calibrated with respect to Ge as internal standard; a_{Ge} = 0.565791 nm at room temperature) using the program STRUKTUR [42]. Quantitative Rietveld refinement was used to determine the atom sites, phase distribution and lattice parameters employing the program FULLPROF [43,44]. Microstructure and chemical composition were analyzed by scanning electron microscopy (SEM) and electron probe microanalysis (EPMA) via an INCA Penta FETx3 – Zeiss SUPRA™55VP equipped with an EDX detector. As a slight shift was noticed by Armbrüster and coworkers [13] between the EXD measurement for $TiSb_2$ ($Ti_{32.9(2)}Sb_{67.1}$) with respect to the more accurate WDX data ($Ti_{33.3(2)}Sb_{66.7}$), all our measurements were corrected against TiSb, $TiSb_2$ and HfSb standards.

X-ray single crystal diffraction (XSCD) data were collected at room temperature on a Bruker APEXII diffractometer equipped with a CCD area detector and an Incoatec Microfocus Source ImS (30 W, multilayer mirror, Mo-K$_\alpha$). Several sets of phi- and omega-scans with 2° scan width were measured at a crystal-detector distance of 3.5 cm (full sphere; 9.9° ≤ 2θ ≤ 72.4°). The crystal structures were solved applying direct methods (SHELXS-97) and refined against F^2 (SHELXL-97-2) [45] within the program OSCAIL [46].

DTA measurements were performed on samples in sealed quartz ampoules up to 1100 °C in a Netzsch STA 409 CD/3/403/5/G. Recordings at temperatures up to 1600 °C were performed in a Netzsch DSC 404 C Pegasus on samples placed in alumina crucibles weld-sealed under 0.2 bar argon in tantalum containers. Both instruments were calibrated in the temperature range from 300 to 1600 °C against pure metal standards supplied by Netzsch to be within ± 1 °C.

For resistivity and low temperature thermal conductivity measurements samples were cut with a low-speed diamond saw into cuboids (~10 × 1.5 × 1.5 mm^3). The density (d_A) was obtained by the Archimedes principle in distilled water, wherefrom the relative density, d_R, was calculated by $d_R = (d_A/d_X)$; d_X is defined as $d_{Xray} = n_V M/VN$, where n_V is number of atoms in the unit cell, M is average of atomic weight, V is the cell volume and N is the Loschmidt number.

Low temperature resistivity measurements were carried out by a standard four-probe a.c. bridge technique in a homemade equipment from 4.2 to 300 K, whereas the high temperature part (300–823 K) was measured in parallel with the Seebeck coefficient with an ULVAC-ZEM3 instrument. Thermal conductivity measurements in the range of 4.2–300 K were performed by a steady heat flow method in a homemade equipment (for details on the homemade equipments for resistivity and thermal conductivity measurements see Refs. [47,48]). The error for both measurements is in the range of 5%. Specific heat was studied with a commercial Quantum Design PPMS (Physical Properties Measurement System) in the temperature range from 2 K to 300 K. A home-made capacitance dilatometer [49] served to acquire thermal expansion coefficients in the temperature range from 4.2 K to 300 K (error less than 5%).

For the measurement of the static hardness we used a microhardness tester (MHT), AD Paar MHT-4, mounted on a Zeiss Axioplan optical microscope employing a load of 2 N, rate of 0.1 N/s and a loading time

of 10 s (referred to as HV0.1). For all collected indentation data (at least 10 indents per sample) the Vickers hardness HV was calculated using the following equation:

$$HV = \frac{2F sin\frac{136°}{2}}{(2l)^2}$$

(1)

where l is the average of the diagonal length for the Vickers indents and F the indentation load. Prior to hardness tests the test samples were polished with a 0.3 mm alumina paste. Elastic properties (Young's moduli (E) and Poisson's ratio (ν)) were obtained via Resonant Ultrasound Spectroscopy (RUS) at room temperature (RT). The error bar for mechanical properties is < 5%.

3. Results and discussion

3.1. Crystal structure of binary compounds in the Ti–Sb system

Rietveld refinements of the binary samples in as-cast state and after annealing at 800 °C and 950 °C confirmed seven structure types as reported in the literature (for details see Table 1): Ti_3Sb (Cr_3Si-type), Ti_2Sb (own type, distorted La_2Sb), Ti_5Sb_3 (β-Yb_5Sb_3), $Ti_{11-x}Sb_{8-y}$ ($Cr_{11}Ge_8$-type), TiSb (NiAs-type), Ti_5Sb_8 (see below) and $TiSb_2$ ($CuAl_2$-type).

The crystal structure of Ti_5Sb_8, was resolved from X-ray single crystal data (Table 2) confirming the structure to be isotypic to $(M,Ti)_5Sb_8$ (M = Zr, Hf, Nb, Mo) [36,37]. Rather elongated ellipsoids for the atom displacement parameters at the Ti3 and Sb2 sites were obtained for Ti_5Sb_8 very similar to those for the respective atom sites located in the structures $(M,Ti)_5Sb_8$ determined by H. Kleinke (see CIF file in the supplementary information in Ref. [36]). This seems to be a common feature of this structure type associated with elongated and

Table 2
X-Ray single crystal data for Ti_5Sb_8; $Zr_{2.6}Ti_{2.4}Sb_8$-type, space group $I4_122$ - No. 98 (redundancy < 10; 9.9 ≤ 2θ ≤ 72.4°). Standardized with program Structure Tidy [78].

Parameter	Ti_5Sb_8
a, c [nm]	0.647593(9), 2.64256(4)
Refinement/EPMA [at.% Sb]	61.5/61.4
Reflections in refinement	1280 F_o > 4σ(F_o) of 1348 total
Number of variables	34
$R_F^2 = \Sigma|F_o^2-F_c^2|/\Sigma F_0^2$	0.0315
R_{Int}	0.0407
w$R2$	0.0635
GOF	1.457
Extinction (Zachariasen)	0.00087(5)
Ti1 in 8c (0,0,z)	z = 0.20283(9)
U_{11}, U_{22}, U_{33}	0.0056(8), 0.0054(8), 0.0122(9)
$U_{23} = U_{13} = 0$, U_{12} [10^{-2} nm^2]	−0.0009(6)
Ti2 in 8c (0,0,z)	z = 0.40168(9)
U_{11}, U_{22}, U_{33}	0.0038(8), 0.0079(9), 0.0070(7)
$U_{23} = U_{13} = 0$, U_{12} [10^{-2} nm^2]	0.0008(8)
Ti3 in 4a (0,0,0)	
$U_{11} = U_{22}$, U_{33}	0.0060(8), 0.026(2)
$U_{23} = U_{13} = 0$, U_{12} [10^{-2} nm^2]	0.0006(9)
Sb1 in 16g (x,y,z)	0.7030(1), 0.1590(1), 0.06173(3)
U_{11}, U_{22}, U_{33}	0.0136(3), 0.0058(2), 0.0080(2)
U_{23}, U_{13}, U_{12} [10^{-2} nm^2]	0.0002(2), 0.0040(2), -0.00008(20)
Sb2 in 8f (x,1/4,1/8)	x = 0.1575(2)
U_{11}, U_{22}, U_{33}	0.0055(3), 0.0237(5), 0.0144(4)
U_{23}, $U_{13} = U_{12} = 0$ [10^{-2} nm^2]	0.0119(4)
Sb3 in 8d (x,x,0)	x = 0.32733(9)
$U_{11} = U_{22}$, U_{33}	0.0061(2), 0.0070(3)
$U_{23} = -U_{13}$, U_{12} [10^{-2} nm^2]	−0.0016(2), 0.0016(2), -0.0002(2)
Residual density; max; min	+ 2.4/-2.3 × 10^3 ē/nm^3
Principal mean square atomic	Ti1 0.0122 0.0064 0.0046
displacements U [10^{-2} nm^2]	Ti2 0.0081 0.0070 0.0036
	Ti3 0.0265 0.0065 0.0054
	Sb1 0.0157 0.0061 0.0057
	Sb2 0.0319 0.0062 0.0055
	Sb3 0.0090 0.0060 0.0044

"bond-loss" coordination polyhedra for these sites. Although single crystal data of Ti_5Sb_8 appear fully consistent with the structure type of $(M,Ti)_5Sb_8$, Rietveld refinement of X-ray powder diffraction data of Ti_5Sb_8, however, reveals a distortion of the Ti_5Sb_8 structure that appears in peak splitting and off-set positions for some reflections.

The tetragonal modification of Ti_3Sb, reported by Kjekshus to be closely related to the β-W-type ($\equiv W_3O$-type, better known as Cr_3Si-type) [25], has been eliminated from the phase diagram as an impurity stabilized phase [31]. Its structure corresponds to the W_5Si_3-type, which has been fully characterized for ternary $Ti_5Si_{1.32}Sb_{1.68}$ [26]. Consequently, this tetragonal phase was not observed in our study, neither in the as-cast sample nor after annealing in alumina crucibles, placed in evacuated silica tubes at 800 °C and 950 °C. Obviously these temperatures are too low for an interaction with these cladding materials. Similarly, $Ti_{5-x}Sb_{4-y}$ with Ti_5Ga_4-type was not observed in the present work and the sample with the composition assigned for this phase, $Ti_{4.80}Sb_{3.29}$ [40], contains $Ti_{11-x}Sb_{8-y}$ ($Cr_{11}Ge_8$-type) and Ti_5Sb_3 (β-Yb_5Sb_3) in all states investigated (as-cast, and after annealing at 950 °C and at 800 °C).

Binary Ti_3Sb shows an extensive homogeneity region ranging from 21.9 to 24.4 at.% Sb. The Rietveld refinement of the Sb-rich phase reveals a complete atom order in the Cr_3Si-type whilst the Ti-rich composition is better described by a random mixture of Ti/Sb in the 2a site ($Ti_{3+x}Sb_{1-x}$) than with an Sb defect in this site (Ti_3Sb_{1-x}). Detectable homogeneity regions were also established for $Ti_{11-x}Sb_{8-y}$ (from 41.9 to 43.0 at.% Sb) and TiSb (from 49.5 to 50 at.%), whilst for all another phases the extension of the single phase regions is below 0.3 at.%.

Crystallographic data on all binary phases from the literature and from the current investigation are summarized in Table 1.

3.2. Constitution of the Ti–Sb system

Phase equilibria in the Ti–Sb system were derived from SEM, EPMA (EDX) and XPD data on alloys in as-cast state and after annealing at 950 °C, 800 °C and 600 °C. DTA measurements for the samples with an antimony content above 60 at.% Sb were performed in evacuated silica ampoules at temperatures up to 1100 °C (Netzsch STA 409 CD/3/403/5/G). Measurements in a heating-cooling regime with the rate of 5 °C min^{-1} were repeated for 2 to 3 times in order to ensure reproducibility and to elucidate the crystallization behavior of the alloys. Inspection of the samples after DTA by EPMA shows no contamination for the composition range $TiSb_2$–Sb whilst for Ti richer samples the formation of a Si containing phase was observed, and therefore only the temperatures recorded during heating of the first DTA run were considered. Samples with higher titanium content melt at higher temperatures, and therefore DTA investigations were performed in tantalum crucibles weld-sealed under 0.2 bar argon. Based on our SEM and EPMA data the lowest melting temperature was expected for the two phase region (Ti) + Ti_3Sb and therefore DTA was performed first for sample $Ti_{85}Sb_{15}$ in the temperature range from 700 to 1550 °C. Three thermal effects were detected: at 820 °C (transformation β-Ti ↔ α-Ti), 1306 °C (solidus) and 1450 °C (liquidus). The sample after DTA was strongly attached to the crucible due to a strong interaction with tantalum. Therefore, in order to avoid possible destruction of the crucible and the DTA setup, an additional internal alumina crucible was used for all other samples. The inspection of these samples after DTA by SEM and EPMA shows some interaction of the melt with Al_2O_3, and therefore only the first thermal effect recorded for the first heating run was considered to be relevant and was assigned to the solidus temperature.

The microstructure of the as-cast sample $Ti_{85}Sb_{15}$ shows primary crystallization of titanium that dissolves about 11 at.% Sb and Ti_3Sb with the composition $Ti_{78.1}Sb_{21.9}$ (Fig. 3a). A close examination of the primary grains discloses precipitations inside of them suggesting a β-Ti ↔ α-Ti transformation during cooling. XPD of this sample in as-cast state and after annealing at 950 °C (Fig. 3b) reveals only the low temperature modification of titanium α-Ti and Ti_3Sb confirming a complete transformation of β-Ti into α-Ti during quenching. Consequently, the thermal effect observed by DTA at 820 °C was assigned to this transformation. EPMA shows that the homogeneity region of the Ti based solid solution decreases from 11.1 at.% Sb at solidus temperatures (assigned after EPMA of as-cast samples) to 7 at.% Sb in the samples annealed at 600 °C. These data agree well with the solubility region as proposed by Murray [31]. Primary crystallization of Ti_3Sb observed in the as-cast sample $Ti_{80}Sb_{20}$ (Fig. 3c) is continued by the crystallization of a eutectic ℓ ↔ (Ti) + Ti_3Sb at 18.7 at.% Sb. The composition of Ti_3Sb changes from 22.8 at.% Sb inside of the grains to 21.9 at.% Sb in the phase in equilibrium with the eutectic. After annealing at 950 and 800 °C, the eutectic coagulates (Fig. 3d), and the compositions of Ti_3Sb in equilibrium with the titanium based solid solution is almost temperature independent and equals 21.8(2) at.% Sb. It is interesting to note that in the sample annealed at 950 °C we observed the formation of a Ti_2Sb layer with a thickness of about 50 μm on the surface of the specimen. A similar formation of such a surface layer with an Sb-enriched phase was also encountered for all other samples annealed at 950 °C. Ti_2Sb was found as primary phase in the as-cast sample $Ti_{75}Sb_{25}$ (Fig. 3e) and the crystallization continues with the formation of Ti_3Sb ($Ti_{76.4}Sb_{23.6}$) and small grains of a non-equilibrium Ti-based solid solution. After annealing at 950 °C this non-equilibrium phase does not disappear completely, but also coagulates slightly (Fig. 3f), and in addition, one can see tiny black precipitates formed inside the grains of Ti_3Sb. The crystallization of the Ti-based solid solution from the last portion of the liquid is also noticed in the sample with nominal composition Ti_2Sb. The SEM image of this sample (Fig. 3g) clearly indicates primary crystallization of Ti_5Sb_3 and peritectic formation of Ti_2Sb. The Ti-based solid solution almost vanishes after annealing at 950 °C (Fig. 3h), and DTA of this sample records a solidus temperature of 1422 °C. Taking into account the crystallization behavior discussed above, the existence of two peritectic reactions, ℓ + Ti_5Sb_3 ↔ Ti_2Sb, ℓ + Ti_2Sb ↔ Ti_3Sb, and one eutectic reaction, ℓ ↔ Ti_3Sb + β-Ti, (Fig. 2b) becomes obvious. The solidus temperatures corresponding to these reactions, determined by DTA, are 1422 °C, 1375 °C and 1306 °C, respectively. Binary Ti_5Sb_3 forms congruently (Fig. 3i), and no thermal effect was recorded in this sample up to 1600 °C (the high-temperature limit of the instrument). Ti_5Sb_3 is the only compound that melts congruently in this system. Thus the sample with the composition $Ti_{58}Sb_{42}$, (actually reported to be single-phase $Ti_{11-x}Sb_{8-y}$ at $Ti_{10.8}Sb_{7.7}$ [35]) confirmed to be single-phase after annealing at 950 °C, whereas in the as-cast state it shows primary crystallization of Ti_5Sb_3, of secondary $Ti_{11-x}Sb_{8-y}$ and a tiny amount of a phase with the composition $Ti_{53}Sb_{47}$ (Fig. 3j). Please note that this composition is close to $Ti_{1.2}Sb$ ($Ti_{55}Sb_{45}$) [25] and may be assumed to be identical with $Ti_{11-x}Sb_{8-y}$ (see Table 1). Considering the sharp phase boundaries between these two phases (see Fig. 3j) it is obvious that $Ti_{11-x}Sb_{8-y}$ is an individual phase. $Ti_{1.2}Sb$ was neither observed in the sample annealed at 950 °C nor in any of the other investigated samples, and is therefore considered to be a high temperature phase or a metastable phase. Accordingly the as-cast sample $Ti_{1.2}Sb$ does not show this phase but subsequent crystallization of $Ti_{11-x}Sb_{8-y}$, TiSb and of Ti_5Sb_8 (see Fig. 3k). The specimen annealed at 950 °C consists of $Ti_{11-x}Sb_{8-y}$ + TiSb (see Fig. 3l). Although TiSb was earlier claimed to melt congruently (see Fig. 2a) [31,50], we cannot confirm this observation. The as-cast sample (see Fig. 3m) contains this phase, but it solidifies peritectically after primary crystallization of $Ti_{11-x}Sb_{8-y}$, however, the sample changes to single phase TiSb after annealing at 950 °C. Incongruent formation is also established for Ti_5Sb_8, and alloys of this composition in as-cast state show primary TiSb with subsequent crystallization of Ti_5Sb_8, $TiSb_2$ and (Sb) (see Fig. 3n). The specimen becomes almost single-phase after annealing at 1050 °C, but after additional heat treatment at 950 °C (see Fig. 3o) it contains a non-equilibrium mixture of Ti_5Sb_8, $TiSb_2$ and TiSb. This observation agrees well with the temperature stability range established for this phase by DTA (from 950 °C to 1092 °C). The data on the temperature stability range of
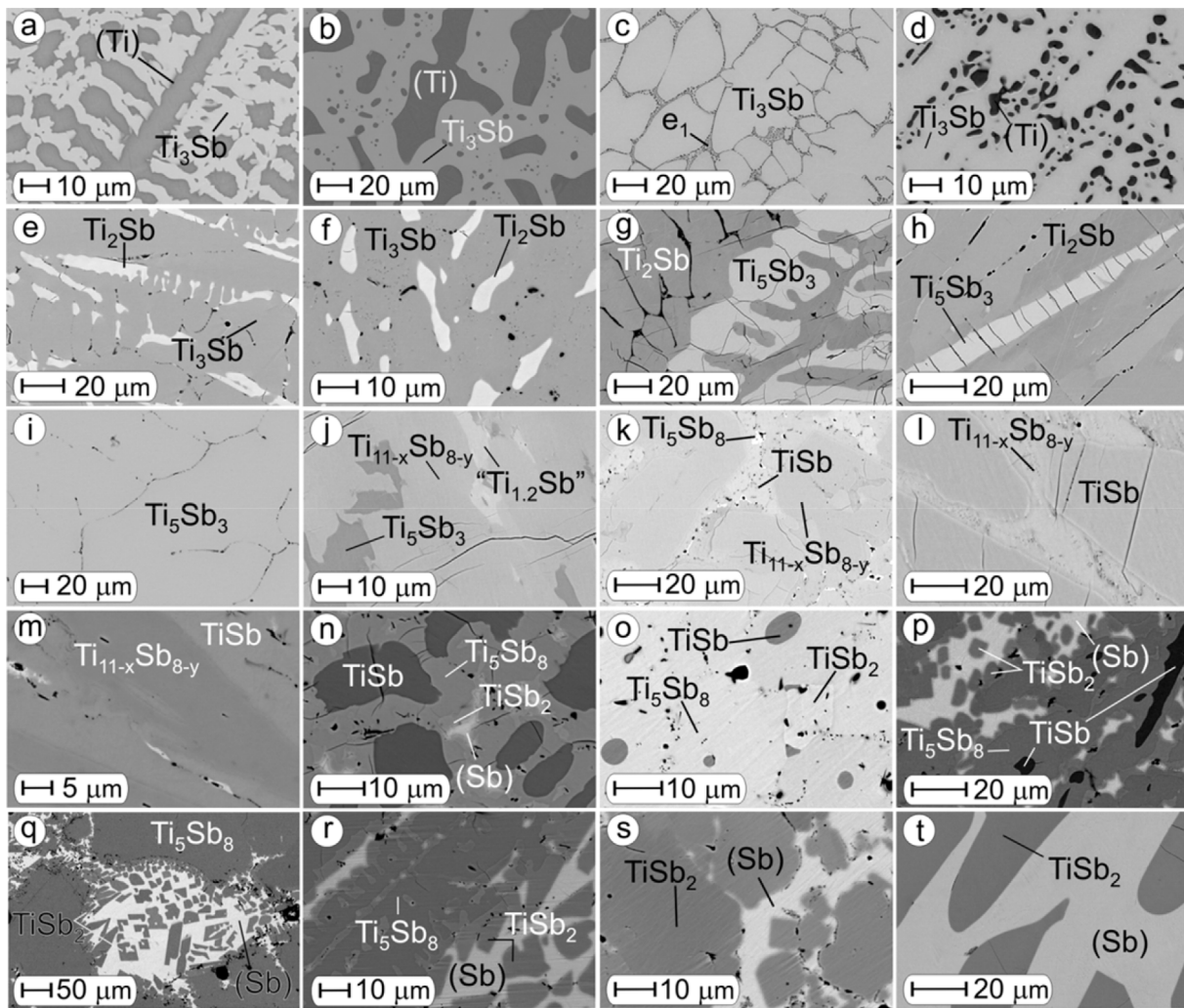
Fig. 3. Selected SEM images for Ti−Sb samples: $Ti_{85}Sb_{15}$, as-cast (a), 950 °C (b); $Ti_{80}Sb_{20}$, as-cast (c), 950 °C (d); Ti_3Sb, as-cast (e), 950 °C (f); Ti_2Sb, as-cast (g), 950 °C (h); Ti_5Sb_3, as-cast (i); $Ti_{10.8}Sb_{7.7}$, as-cast (j); $Ti_{55}Sb_{45}$ ($Ti_{1.2}Sb$), as-cast (k), 950 °C (l); TiSb, as-cast (m); Ti_5Sb_8, as-cast (n), 950 °C (o); $Ti_{35}Sb_{65}$, as-cast (p), 1080 °C (q); $TiSb_2$, as-cast (r); $Ti_{27}Sb_{73}$, as-cast (s), after DTA (t). Codes from "a" to "t" correspond to the respective samples on Fig. 2b.

Ti_5Sb_8 enabled us to grow a single crystal of this high temperature phase for structural investigation (see Sec. 3.1). For this reason the sample $Ti_{35}Sb_{65}$ (which in as-cast state shows the crystallization sequence TiSb, Ti_5Sb_8, $TiSb_2$ and (Sb) (Fig. 3p)) was annealed at 1080 °C, yielding large crystals of Ti_5Sb_8 (Fig. 3q) growing in equilibrium with the Sb-rich melt, which crystallizes with the formation of well shaped small crystals of $TiSb_2$ from the Sb-rich liquid. $TiSb_2$ melts incongruently (Fig. 3r) and forms a degenerated eutectic $\ell \leftrightarrow TiSb_2$ + (Sb) at about 99 at.% Sb (measured in antimony rich samples in the as-cast state (Fig. 3p, r, s), after annealing in equilibrium with the Sb-rich melt (Fig. 3q) and after DTA (Fig. 3t)). These data agree well (a) with the temperature of 620 °C established for this eutectic, (b) with the curvature of the liquidus for primary crystallization of $TiSb_2$, determined by our DTA, as well as (c) with the data of H. Nowotny and J. Pesl [18] on the liquidus temperature of 680 °C for the sample with 1.3 at. % Ti (Fig. 2b).

All the data collected were used to construct for the first time a complete constitution diagram for the binary system Ti−Sb (see Fig. 2b).

3.3. Partial phase diagrams $ZrSb_2$−Sb and $HfSb_2$−Sb

Phase equilibria for the binary Zr−Sb and Hf−Sb systems are summarized in Fig. 4. They were established for the first time based on samples with an antimony content above 65 at.% Sb.

$ZrSb_2$−Sb: Two modifications of $ZrSb_2$ have been reported in the literature: α-$ZrSb_2$ ($TiAs_2$-type) and β-$ZrSb_2$ ($PbCl_2$-type). β-$ZrSb_2$ has been described as an antimony deficient $ZrSb_{1.96}$ [16], but later was proven to be an impurity stabilized phase [20]. A further binary antimonide $Zr_{11}Sb_{18}$ with a composition close to $ZrSb_2$ was also reported [51] and this compound appeared as a primary phase in our arc-melted samples $ZrSb_2$ (Fig. 5a). $ZrSb_2$ with $TiAs_2$ type crystallizes as a secondary phase and a peritectic formation of this phase is obvious from the microstructure in Fig. 5a. The temperature of the corresponding peritectic reaction, ℓ + $Zr_{11}Sb_{18} \leftrightarrow ZrSb_2$, was determined by DTA at 1363 °C. $ZrSb_2$ crystallizes as the primary phase at higher antimony contents (sample $Zr_{25}Sb_{75}$, Fig. 5b), and the curvature of the liquidus for this phase (determined by DTA) defines the composition of the liquid in this peritectic reaction at ∼ 68 at.% Sb.

$HfSb_2$−Sb: Similarly to $ZrSb_2$, literature data infer two structure variants for $HfSb_2$: α-$HfSb_2$ (isotypic to $ZrSb_2$ with $TiAs_2$ type), and β-$HfSb_2$ with the UAs_2 type [21]. Later β-$HfSb_2$ was recognized to be Hf_5Sb_9 [22], which in fact is a $a = a_0 \times \sqrt{5}$ superstructure of the UAs_2-type. Differential scanning calorimetry analyses [22] revealed that Hf_5Sb_9 forms endothermally out of $HfSb_2$ at around 1020 °C. Although the authors were unable to synthesize Hf_5Sb_9 below 1000 °C, Hf_5Sb_9 was obtained in quantitative yields after heating the $HfSb_2$ sample to 1075 °C as well as after arc-melting $HfSb_2$. Annealing of Hf_5Sb_9 at 750 °C results in slow decomposition under formation of $HfSb_2$ + HfSb [52].
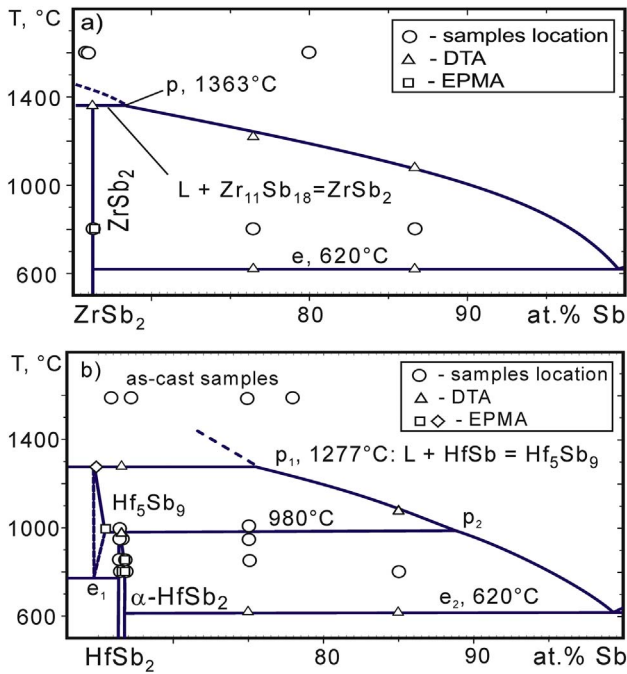
Fig. 4. Phase diagrams Zr–Sb (a) and Hf–Sb (b).

As-cast HfSb$_2$ (Fig. 5c) shows primary crystallization of HfSb (ZrSb-type), secondary Hf$_5$Sb$_9$ (own structure type) and antimony with less than 0.2 at.% Hf. After annealing at 850 °C the high temperature phase Hf$_5$Sb$_9$ completely transforms into orthorhombic HfSb$_2$ (TiAs$_2$ type structure). HfSb$_2$ with the TiAs$_2$ type is also observed in HfSb$_2$ samples prepared by isothermal reaction from pure elements at 800 °C (Fig. 5d), but traces of Hf$_5$Sb$_9$ were observed by XPD in the HfSb$_2$ sample prepared at 800, 850 °C and 950 °C. This observation contradicts literature data [22,52] on the existence of Hf$_5$Sb$_9$ at temperatures above 1020 °C. The second discrepancy arises from our DTA data of HfSb$_2$ revealing two thermal effects at 980 °C and at 1277 °C. Considering the microstructure of the as-cast sample, a temperature of 1277 °C was assigned to the peritectic reaction, ℓ + HfSb $\leftrightarrow$ Hf$_5$Sb$_9$ (p$_1$), whilst the temperature of 980 °C (ℓ + Hf$_5$Sb$_9$ $\leftrightarrow$ HfSb$_2$ (p$_2$)) appears to be significantly lower than 1020 °C reported in the literature for the sample with the same composition [22,52]. Possible sources for these discrepancies become obvious from the phase diagram constructed for the system (Fig. 4). In the temperature range from 980 °C to 1277 °C, Hf$_5$Sb$_9$ occurs in all the samples in equilibrium with antimony. The authors of [22]

reported a change for the composition of HfSb$_2$ due to evaporation of about 5.5 at.% Sb during DTA: with changing composition any temperature in the temperature range from 980 °C to 1277 °C might be recorded under such conditions (actually a temperature of 1020 °C was reported by Refs. [22,52]). Our samples for DTA were sealed either in silica tubes or in tantalum tubes, both preventing any loss of antimony. In order to prove the temperature of 980 °C, we annealed the sample Hf$_{25}$Sb$_{75}$ at 950 and 1005 °C: no Hf$_5$Sb$_9$ was recorded in the first case whilst XPD of the sample, annealed at 1005 °C, shows significant amounts of this phase. On the other hand, single phase Hf$_5$Sb$_9$ exists at much lower temperatures. The authors [22,52] report on a very slow decomposition of Hf$_5$Sb$_9$ to HfSb$_2$ and HfSb at 750 °C, and these data in combination with our observation on the presence of Hf$_5$Sb$_9$ in (Sb)-free samples prepared at 800 °C define the eutectoid decomposition of this phase Hf$_5$Sb$_9$ $\leftrightarrow$ HfSb$_2$ + HfSb (e$_1$) at 775 $\pm$ 25 °C (Fig. 4).

The solubility of Zr and Hf in (Sb) in all samples investigated is below 0.2 at %. The eutectic structure that should correspond to the invariant equilibrium ℓ $\leftrightarrow$ MSb$_2$ + (Sb) was never observed suggesting a degeneration of this reaction with the composition of the eutectic liquid at about 1 at. % Zr or Hf.

3.4. Transport properties of MSb$_2$ (M = Ti, Zr, Hf)

Proper pieces of large samples ($\sim$0.75 cm^3) were used for the measurement of physical properties. XPD and Rietveld refinement for MSb$_2$ (M = Ti, Zr, Hf) confirm single-phase condition as well as the tetragonal structure for TiSb$_2$ (S.G. *I4/mcm*) and the orthorhombic structure (S.G. *Pnnm*) for ZrSb$_2$ and HfSb$_2$, respectively. Lattice parameters and compositions of these binary compounds are listed in Table 3.

3.4.1. Electrical resistivity and Seebeck coefficient

Electrical resistivity measurements, carried out between 4.2 and 823 K for MSb$_2$ (M = Ti, Zr, Hf), are summarized in Figs. 6 and 7. The low temperature resistivity (from 4.2 to 300 K) of polycrystalline TiSb$_2$ is compared (Fig. 6) with the average resistivity ($\rho_{av} = (2\rho_a + \rho_c)/3$) calculated from the resistivities reported by Armbrüster et al. [15] for the two crystallographic directions (a, c) of a single crystal. Obviously, both curves show very similar temperature dependencies (Fig. 6), but the resistivity of the polycrystalline sample is about 4% higher due to additional scattering of electrons on grain boundaries. The temperature dependent resistivity for ZrSb$_2$ agrees well with the data of Garcia et al. [16] but shows about 3% lower values. The electrical resistivity for all samples exhibits metallic behavior, and therefore the experimental ρ(T) curves can be accounted for by a combination of (i) a residual electrical resistivity, ρ_0, (ii) the contribution due to electron-phonon scattering, as described by the Bloch-Grüneisen relation, ρ_{BG}(T), and (iii) a Mott-Jones term, which accounts for scattering processes of electrons on a narrow d-band in the electronic density of states (DOS) near the Fermi energy E$_F$:

$$\rho_T = \rho_0 + R\left(\frac{T}{\theta_D}\right)^5 \int_0^{\frac{\theta_D}{T}} \frac{x^5}{(e^x - 1)(1 - e^{-x})} + AT^3. \tag{2}$$

ρ_0 is the residual resistivity owing to scattering of electrons on static defects in the crystal lattice and impurities; *R* is the electron-phonon interaction parameter; θ_D is the Debye temperature and A is a material dependent constant in the Mott-Jones term. Least squares fits according to Eqn. (2) are shown in Fig. 6 as solid lines, revealing a convincing agreement between the experiment and the model selected.

Fig. 7 shows the fit according Eqn. (2) for the electrical resistivity for the entire temperature range from 4.2 K to 823 K measured on two different instruments. The Debye temperatures obtained for TiSb$_2$, ZrSb$_2$ and HfSb$_2$, are 314 K, 279 K and 245 K, respectively, decreasing with the increase of the ordinal number in this series of compounds and agree with those obtained for the fit below room temperatures.

The temperature dependent Seebeck coefficients (insert in Fig. 7) of TiSb$_2$ and ZrSb$_2$ show an almost continuous rise of S(T) in the range
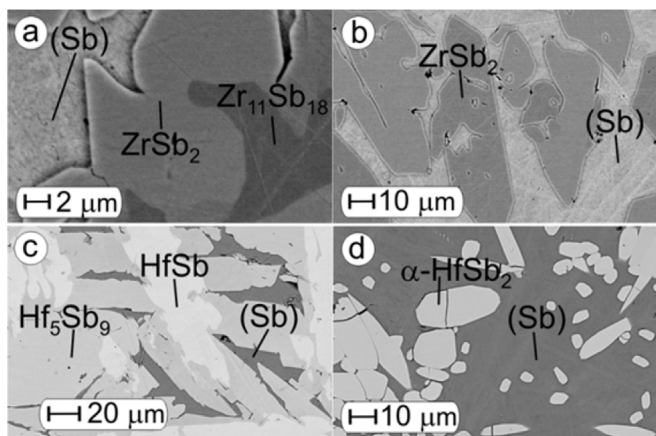

Fig. 5. Selected SEM images for Zr–Sb and Hf–Sb samples: ZrSb$_2$, as-cast (a); Zr$_{25}$Sb$_{75}$, as-cast (b); HfSb$_2$, as-cast (c); Hf$_{25}$Sb$_{75}$, reacted at 800 °C (d).

Table 3
Physical and mechanical properties of MSb_2 (M = Ti, Zr, Hf).

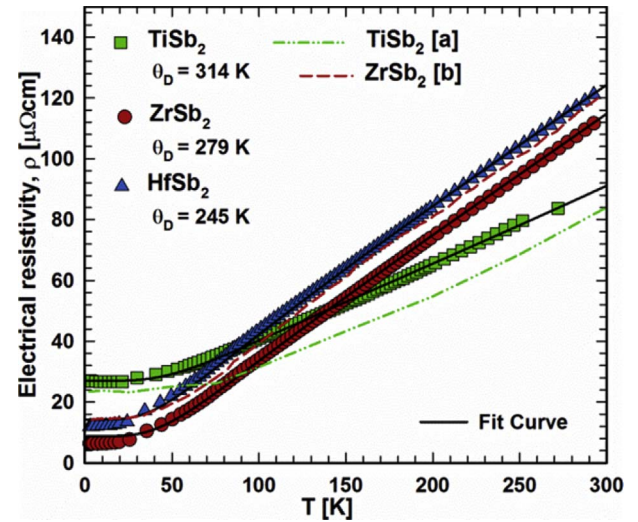| Phase/Parameter	$TiSb_2$	$ZrSb_2$	$HfSb_2$
EPMA [at. %]	$Ti_{34.3}Sb_{65.7}$	$Zr_{33.8}Sb_{66.2}$	$Hf_{32.9}Sb_{67.1}$
Space group	*I4/mcm*	*Pnnm*	*Pnnm*
Structure type	$CuAl_2$	$TiAs_2$	$TiAs_2$
a [nm]	0.66511(4)	0.9957(1)	0.9893(3)
	see Table 1	0.9968(5)[17],	0.9869(5)[17],
		0.99672(6)[79],	0.98781(5)[79],
		0.9963(2)[19],	0.98503(12)[82]
		0.9947(4)[80],	
		0.9919(5)[81]	
b [nm]	0.66511(4)	1.495(3)	1.4975(4)
	see Table 1	1.4974(14)[17],	1.4981(12)[17],
		1.49684(8)[79],	1.49890(9)[79],
		1.4963(3)[19],	1.49629(2)[82]
		1.4952(4)[80],	
		1.4906(6)[81]	
c [nm]	0.58067(5)	0.38775(6)	0.38496(3)
	see Table 1	0.3878(3)[17],	0.3848(3)[17],
		0.38813(3)[79],	0.38506(3)[79],
		0.38779(7)[19],	0.38403(4)[82]
		0.3875(5)[80],	
		0.3876(3)[81]	
d [g/cm³]	7.52	7.62	9.71
d_R [%]	99.6	98.6	98.6
A [$10^5 K^{-3}s^{-1}$]	0.8	1.0	2.1
B [$K^{-4}s^{-1}$]	242	1140	1870
C [$10^8 s^{-1}$]	5.7	13.8	5.9
D [$10^7 K^{-1}s^{-1}$]	3.4	1.6	6.0
F [10^{-6} mW/cmK⁴]	2.4	1.0	1.5
θ_D [K] (RUS) Eqn. 9	335	330	315
Eqn. (2) (ρ)	314	279	245
Eqn. (3) (λ_{ph})	300	259	250
Eqn. (5) (α)	336	270	266
Eqn. (6) (C_p)	344	302	276
Eqn. (7) (C_p)	363	313	270
Junod fit	300	270	251
θ_E [K], Eqn. (7)(C_p)	125/60	109	105
Junod fit {width}	121{13}/56{8}	118{51}	111{47}
Eqn. (5) (α)	127	115	106
α [10^{-6} K^{-1}]	12.9	9.7	10.1
C_p (RT) [J/mol.K]	68.4	74.8	74.1
γ [mJ/mol.K^2], Eqn. 6	1.73	1.48	1.58
β [mJ/mol.K^4], Eqn. 6	0.1437	0.2122	0.2766
HV [kp/mm²] (MHT)	1189	1241	1380
E [GPa] (RUS)	141.7 (2)	135.7 (3)	136.4 (2)
ν (RUS)	0.242(3)	0.243(3)	0.247(3)
G [GPa] (RUS)	57	55	55
B [GPa] (RUS)	91	88	90
B/G	1.60	1.60	1.64
v_L [m/s] (RUS)	4720	4593	4095
v_T [m/s] (RUS)	2754	2676	2373
v_m [m/s] (RUS)	3055	2969	2634
K_C [MPa m$^{1/2}$]	0.95	1.1	1.2

Fig. 6. Temperature dependent electrical resistivity as a function of temperature for MSb_2 (M = Ti, Zr, Hf). The solid line is a fit to Eqn. (2). a – Ref. [15], b – [16].
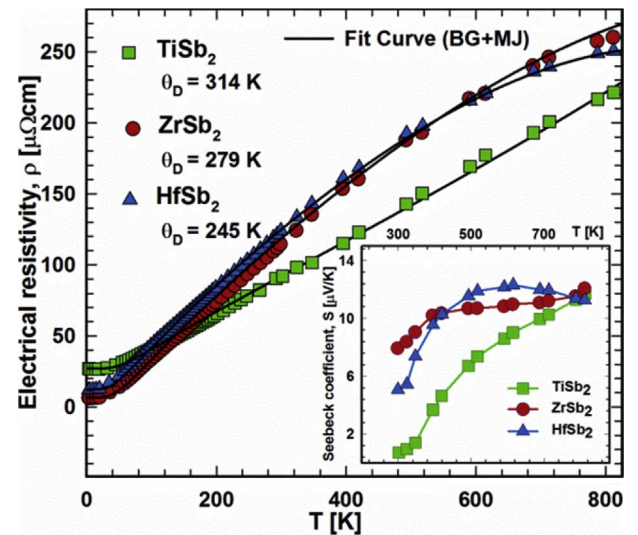

Fig. 7. Temperature dependent electrical resistivity and Seebeck for MSb_2 (M = Ti, Zr, Hf). The solid line is a fit to Eqn. (2).

$\lambda_{ph}(T) = \lambda_{meas.}(T) - \lambda_e(T)$ assuming the validity of the Wiedemann-Franz law, with the electron part of the thermal conductivity $\lambda_e(T) = L(T)T/\rho(T)$. The Lorenz number L(T) was derived from the measured Seebeck coefficient values at room temperature, and the Fermi-integrals as proposed by D.M. Rowe et al. [53].

Quantitatively, the phonon thermal conductivity can be described employing Callaway's model [54,55].

$$\lambda_{ph} = \frac{k_B}{2\pi^2 v_s}\left(\frac{k_B T}{\hbar}\right)^3 \int_0^{\frac{\theta_D}{T}} \frac{\tau_c x^4 e^x}{(e^x - 1)^2}dx \qquad (3)$$

where $x = \hbar\omega/k_B T$ is dimensionless, ω is the phonon frequency, k_B is the Boltzmann constant, $\hbar$ is the reduced Planck constant, θ_D is the Debye temperature, v_s is the velocity of sound, and τ_c is the overall phonon scattering relaxation time, dependent on Umklapp processes, point defect scattering, impurity scattering, boundary scattering and scattering of phonons by electrons. The overall phonon relaxation rate can thus be written as

$$\tau_c^{-1} = \tau_U^{-1} + \tau_D^{-1} + \tau_B^{-1} + \tau_{ph-el}^{-1} = Ax^2 T^3 e^{-\theta_D/3T} + Bx^4 T^4 + C + DTx, \qquad (4)$$

from 300 to 823 K, whereas a slight maximum at 600 K is encountered for $HfSb_2$. In fact, the electronic structure calculations performed for $TiSb_2$ by Armbrüster et al. [15] revealed a total density of 1.4 states/f.u. (= 3.3 mJ/molK²) at the Fermi energy, E_F, which clearly evidences a metallic state. As indicated by Armbrüster et al. [15], the Fermi energy in $TiSb_2$ should be located near to the edge of the conduction band, slightly above a pseudo-gap. The present experimental result (electrical resistivity and Seebeck coefficient) on this compound, however, indicate a simple metallic state.

3.4.2. Thermal conductivity

Fig. 8 displays the temperature dependent thermal conductivity, $\lambda(T)$, as measured between 4.2 and 300 K for MSb_2 (M = Ti, Zr, Hf). The phonon thermal conductivity, λ_{ph}, was taken from the difference

where A, B, C and D are constants. In order to account for the radiation losses, a T^3-term should be added [56]. A least-squares fit to Callaway's equation (Eqn. (3)), including a term for radiation losses (FT^3), perfectly describes the experimental phonon thermal conductivity with fit parameters for phonon relaxation, Debye temperature and coefficient of radiation losses: all quantities are listed in Table 3. Correction for radiation losses yields the corrected phonon thermal conductivity, $\lambda_{ph-corr}$ (T), and as a consequence the corrected thermal conductivity, λ_{corr} (T) Fig. 8. Debye temperatures of 300 K, 259 K and 250 K were extracted from the fitting curves of phonon thermal conductivity for TiSb$_2$, ZrSb$_2$ and HfSb$_2$, respectively. These values of the Debye temperatures are in fair agreement with those obtained from the Bloch-Grüneisen fit of the resistivity data (Table 3).

3.4.3. Thermal expansion at low temperature

The temperature dependent thermal expansion, $\Delta\ell/\ell_0$, of MSb$_2$ (M = Ti, Zr, Hf) in the range from 4.2 K to 300 K is displayed in Fig. 9. From a linear fit in the region from 175 K to 300 K for TiSb$_2$, ZrSb$_2$ and HfSb$_2$, the linear coefficient α of thermal expansion (CTE) amounts to $\alpha(TiSb_2) = 12.9 \times 10^{-6}$ K^{-1}, $\alpha(ZrSb_2) = 9.7 \times 10^{-6}$ K^{-1} and $\alpha(HfSb_2) = 10.1 \times 10^{-6}$ K^{-1}. The present CTE value of TiSb$_2$ is similar to the average values of Co-based p-type Sb-skutterudites ($\alpha_{av \approx} 11 \times 10^{-6}$ K^{-1}), whilst the CTE's values of ZrSb$_2$ and HfSb$_2$ compounds are close to the average values of Co-based n-type Sb-skutterudites ($\alpha_{av} \approx 9 \times 10^{-6}$ K^{-1}) [57].

For a further analysis, the temperature dependent CTE data in the full temperature range are interpreted in terms of a semi-classical model according to Mukherjee [58], using the Debye approach for the acoustic phonons, and the Einstein approximation for the optical modes, also including the electronic contribution to the average lattice displacement. The length change $\Delta\ell/\ell_{T_0}$ is given by

$$\frac{\Delta l}{l_{T_0}} = \frac{x_T - x_{T_0}}{x_0} \quad x_T = \frac{\gamma}{2}T^2 + \frac{3g}{4c^2}[\varepsilon - G\varepsilon^2 - F\varepsilon^3] \quad (5)$$

$$\varepsilon = \left\{ \left(\frac{3}{p}\right)3k_BT\left(\frac{T}{\theta_D}\right)^3 \int_0^{\frac{\theta_D}{T}} \frac{z^3e^z}{(e^z-1)}dz + \left(\frac{p-3}{p}\right)\frac{k_B\theta_E}{(e^{\theta_E/T}-1)} \right\}$$

where γ is the electronic contribution to the average lattice displacement, θ_D is the Debye temperature, θ_E is the Einstein temperature, and p is the average number of phonon branches actually excited over the temperature range. G, F, c, and g are further material dependent constants. Applying Eqn. (5) to our experimental data yields $\theta_D = 336$ K and $\theta_E = 127$ K for TiSb$_2$, $\theta_D = 270$ K and $\theta_E = 115$ K for ZrSb$_2$ and $\theta_D = 266$ K and $\theta_E = 106$ K for HfSb$_2$ (see Fig. 9, Table 3). The Debye temperature via thermal expansion for TiSb$_2$ is slightly larger than the values gained from fits to the electrical resistivity and thermal conductivity; those for ZrSb$_2$ and HfSb$_2$ are the same within the error bar.

3.4.4. Specific heat at low temperature

Figs. 10 and 11 display the temperature dependent specific heat. A smooth $C_p(T)$ dependence is obtained for all three samples (Fig. 10), without any sign of a significant phase transition in the temperature range from 2 K to room temperature. The experimental C_p values at room temperature are 68.4 J/mol.K, 74.8 J/mol.K and 74.1 J/mol.K for TiSb$_2$, ZrSb$_2$ and HfSb$_2$, respectively. The specific heat of the compounds MSb$_2$ (M = Ti, Zr, Hf) at low temperatures follows the behavior of simple solids as accounted for by Eqn. (6),

$$C_p = \gamma T + \beta T^3 \text{ and } \beta = (12qR\pi^4)/(5\theta_D^3) \quad (6)$$

where γ is the Sommerfeld constant and β corresponds to the low temperature limit of the Debye temperature, q is the number of atoms in the formula unit.

Fitting the low temperature specific heat C_p/T vs T^2 of TiSb$_2$ (see Fig. 10b) reveals $\gamma = 1.73$ mJ/molK^2 and $\beta = 0.1437$ mJ/molK^4 which
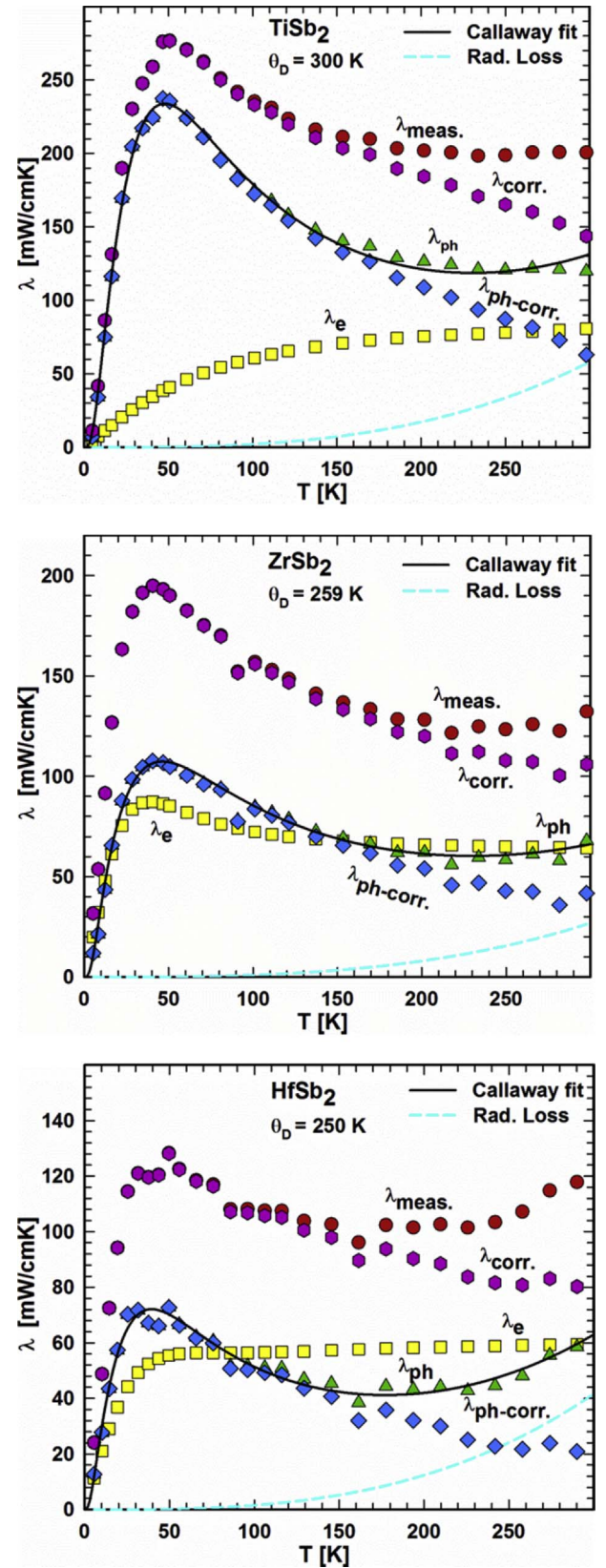

Fig. 8. Temperature dependent thermal conductivity at low temperatures for MSb$_2$ (M = Ti, Zr, Hf).

refers to a Debye temperature $\theta_D^{LT} = 344$ K. The values of the Sommerfeld constant for ZrSb$_2$ and HfSb$_2$ are $\gamma = 1.48$ and 1.58 mJ/molK^2, respectively (see Fig. 10b). The coefficient $\beta = 0.2122$, 0.2766 mJ/molK^4 for ZrSb$_2$ and HfSb$_2$ is slightly higher than for TiSb$_2$, referring to
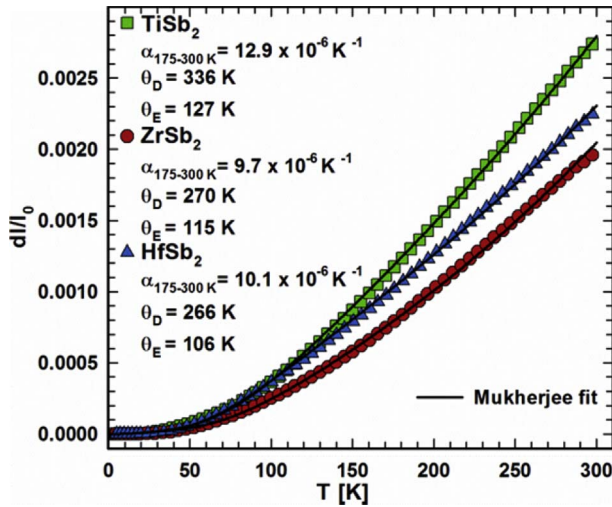
Fig. 9. Temperature dependent thermal expansion for MSb_2 (M = Ti, Zr, Hf). The solid lines are fits to Eqn. (5).

a lower Debye temperature, θ_D^{LT} = 302 and 276 K, respectively (see Table 3). Overall, the very moderate Sommerfeld values indicate compounds with very small values of the electronic density of states (eDOS) right at the Fermi energy.

In a second step we employed the model of Junod [59,60], to achieve a better understanding of the approximate phonon density of states (PDOS), $F(\omega)$ for the two different structure types of the MSb_2 compounds (M = Ti, Zr, Hf). It was shown that a certain functional of the lattice specific heat, particularly $5/4R\pi^4 C_{ph}T^{-3}$ takes the form of convolutions of the phonon spectrum, in this case $\omega^{-2}F(\omega)$ for ω = 4.93 T. The electronic part of the specific heat was subtracted from the total specific heat and the resulting lattice heat capacity is plotted in Fig. 11 versus a logarithmic temperature scale. The PDOS, obtained by fitting with the Junod model to the experimental lattice heat capacity data, is drawn as solid blue line in Fig. 11. In addition to the Debye function with θ_D = 300 K, the phonon spectrum of $TiSb_2$ requires 2 E modes, θ_{E1} = 56 K with a spectral width (w) of 8 K and θ_{E2} = 121 K with a spectral width of 13 K. In contrast to $TiSb_2$, where 2 E modes have narrow widths, the phonon spectra of $ZrSb_2$ and $HfSb_2$ consist of a single Einstein mode with a relatively large width: for $ZrSb_2$ one Einstein mode, θ_{E1} = 118 K with a width of 51 K was extracted from the least squares fits, whereas for $HfSb_2$ θ_{E1} = 111 K with a width of 47 K was obtained. The corresponding Debye temperatures for 1 E mode are slightly lower (θ_D = 270 K and 251 K for $ZrSb_2$ and $HfSb_2$, respectively).

For the complete temperature range, experimental data $C_p(T)$ are accounted for by the following equation:

$$C_P(T) = C_{el} + C_{ph} = \gamma T + 9R\left(\frac{T}{\theta_D}\right)^3 \int_0^{\frac{\theta_D}{T}} \frac{e^x x^4}{(e^x - 1)^2} dx + \sum_{i=1,2} c_i \frac{R\left(\frac{\theta_{Ei}}{2T}\right)^2}{sinh^2\left(\frac{\theta_E}{2T}\right)}$$

(7)

Here, $C_{ph}(T)$ is taken into account, using the Debye model (three acoustic branches) and adding 3p-3 optical Einstein branches (p is the number of atoms in the primitive cell) [61]. In the case of $TiSb_2$ with 6 atoms in the primitive cell the number of optical Einstein branches is 15, while for $ZrSb_2$ and $HfSb_2$ with 24 atoms/primitive cell 69 branches were used. From 2 to 300 K, $C_p(T)$ can be well fitted employing Eqn. (7) (see Fig. 10). For the Sommerfeld constants in Eqn (7) we used those obtained from Eqn. (6) at low temperature.

Considering the fit with Junods' model (Fig. 11) 2 E modes with certain widths were used for $TiSb_2$ while only 1 E mode was used for $ZrSb_2$ and $HfSb_2$. The extracted Einstein and Debye temperatures from
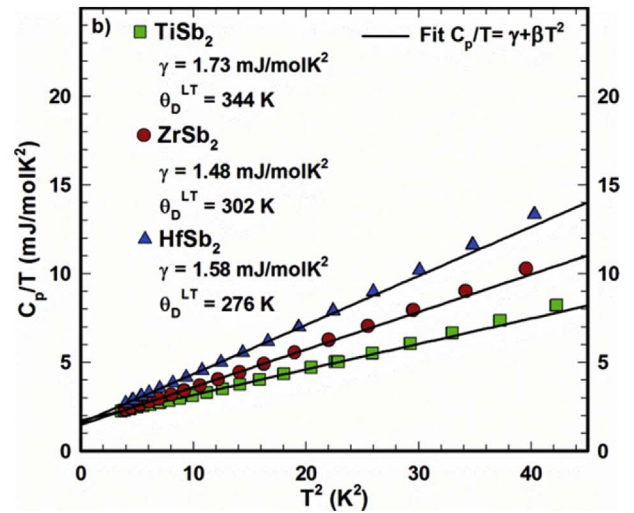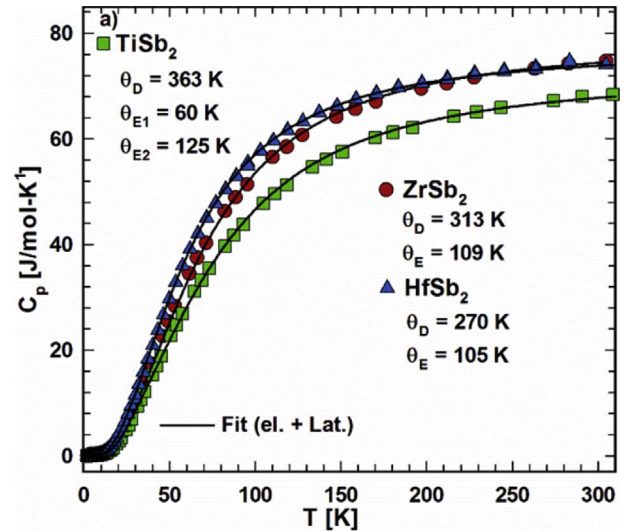

Fig. 10. Fits of the ttemperature dependent specific heat for MSb_2 (M = Ti, Zr, Hf). The solid lines are fits according to Eqns. (6) and (7).

Eqn. (7) agree well with values obtained by various other methods (Table 3). The smaller Debye temperature of $HfSb_2$ compared to the isostructural $ZrSb_2$ complies well with the higher mass of hafnium.

3.5. Mechanical properties of MSb_2 (M = Ti, Zr, Hf) at room temperature

Resonant ultrasound spectroscopy (RUS) was employed to directly derive the elastic properties, Young's modulus (E) and the Poisson ratio (ν), of the compounds MSb_2 (M = Ti, Zr, Hf) at room temperature. For an isotropic medium, the shear modulus (G) and bulk modulus (B) can be calculated using equations (8):

$$G = \frac{E}{2\nu + 1} \text{ and } B = \frac{E}{3(1 - 2\nu)}$$

(8)

The experimentally derived as well as the calculated elastic moduli of MSb_2 (M = Ti, Zr, Hf) are summarized in Table 3. With E = 172, 188 and 161 GPa for $TiSb_2$, $ZrSb_2$ and $HfSb_2$ respectively, the values are higher than those for the half Heusler alloys TiNiSn (E = 142 GPa), ZrNiSn (E = 136 GPa) and HfNiSn (E = 136 GPa) [62] as well as for filled skutterudites for which Young's moduli are in the range of 100–140 GPa [57]. The ratio B/G ~1.6 indicates that all three samples
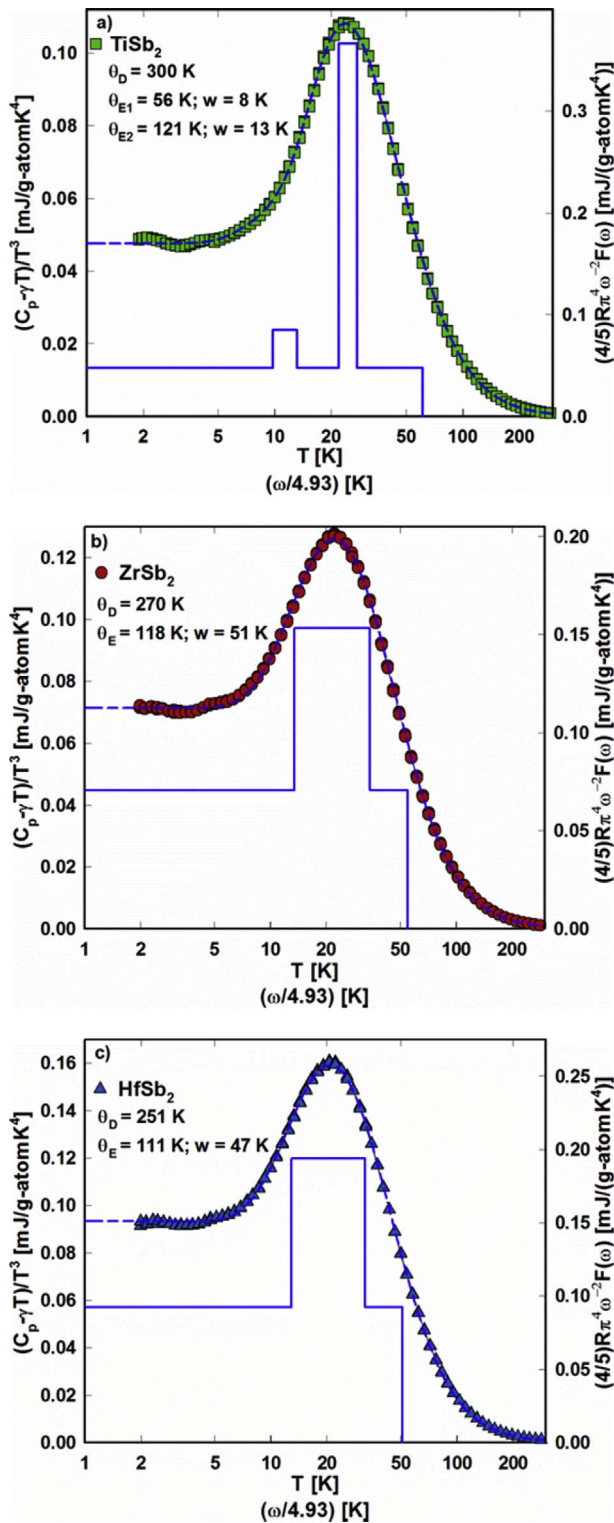
Fig. 11. Temperature-dependent specific heat of MSb$_2$ (M = Ti, Zr, Hf) plotted as C$_{ph}$/T^3 versus ln T. Least-squares fits were made to the experimental data using the Junod model described in the text. The blue solid lines (referring to the right axis) represent the corresponding phonon spectral functions F(ω) plotted as 4/5Rπ^{4}ω^{-2} F(ω) versus ω/4.93 with ω in Kelvin. (For interpretation of the references to colour in this figure legend, the reader is referred to the Web version of this article.)

comply with the criterion of Pugh [63] i.e. a material is brittle if the ratio B/G < 1.75.

Debye temperatures were calculated using Anderson's equation (9) [64].

$$\theta_D = \frac{h}{k_B}\left(\frac{3qNd}{4\pi M}\right)^{\frac{1}{3}}v_m, \quad v_m = \left[\frac{1}{3}\left(\frac{2}{v_T^3} + \frac{1}{v_L^3}\right)\right]^{-\frac{1}{3}},$$

$$v_L = \left(\frac{3B+4G}{3d}\right)^{\frac{1}{2}} \text{and } v_T = \left(\frac{G}{d}\right)^{\frac{1}{2}}$$

(9)

where h is the Plank's constant, k$_B$ is Boltzmann's constant, N is Loschmidt's number, d is the density, M is the molecular weight, and q is the number of atoms in the formula unit. Also with this method the Debye temperatures of 335, 330 and 315 K decrease in the sequence TiSb$_2$, ZrSb$_2$ and HfSb$_2$ (see Table 3), but whereas for TiSb$_2$ they are in the same range as gained via various other methods (electrical resistivity, thermal conductivity, thermal expansion), for ZrSb$_2$ and HfSb$_2$ they are slightly higher.

Hardness measurements from a microhardness tester are listed in Table 3. Hardness values for TiSb$_2$, ZrSb$_2$ and HfSb$_2$ (HV = 1189, 1241, 1380 respectively) do not differ too much but in contrast to the Debye temperatures they increase with increase of the ordinal number in the series. The hardness values are higher than those for half-Heusler alloys (HV(TiNiSn) = 999, HV(ZrNiSn) = 1009, HV(HfNiSn) = 984 [62]) and much higher than those of filled skutterudites (HV = 300–500 [57]).

Fracture toughness, K$_C$, is used to test the resistance of a material to crack propagation and is therefore an important property of a material for many design applications. For measurements of K$_C$ usually the single-edge notched beam test method is used. In this work K$_C$, also called fracture resistance, can be calculated from the relation [65,66].

$$K_C = \beta\left(\frac{E}{HV}\right)^{1/2}\frac{F}{c^{3/2}}$$

(10)

where E is the Young's modulus, HV is the hardness, F is the indentation load, c is the radial crack length from the centre of the Vickers indentation and β is a function of the indenter angle, which for Vickers indentation is β = 0.016(4). As the results of K$_C$ via the single-edge notched beam test method and the calculated K$_C$ are within the error bar the same, in many publications fracture resistance is taken as fracture toughness. Fracture resistance values, K$_C$, for TiSb$_2$, ZrSb$_2$ and HfSb$_2$ are 0.95, 1.1 and 1.2 MPa m$^{1/2}$, respectively, increasing in parallel with increasing hardness values. They are lower than those of n-type half Heusler alloys (1.8–2.3 MPa m$^{1/2}$) or skutterudites [57,62].

4. Summary and conclusions

In order to provide further insight to the chemical interactions (mainly reactions with antimony) in thermoelectric joints of a hot metal electrode with p- and n-type skutterudites, in this work we constructed for the first time a complete phase diagram for the Ti−Sb system as well as partial phase diagrams (> 65 at.% Sb) for the systems Zr−Sb and Hf−Sb.

For the binary system Ti−Sb we confirmed seven structure types: Ti$_3$Sb (Cr$_3$Si-type), Ti$_2$Sb (own type, distorted La$_2$Sb), Ti$_5$Sb$_3$ (βYb$_5$Sb$_3$), Ti$_{11-x}$Sb$_{8-y}$ (Cr$_{11}$Ge$_8$-type), TiSb (NiAs-type), Ti$_5$Sb$_8$ (Zr$_{2.6}$Ti$_{2.4}$Sb$_8$-type) and TiSb$_2$ (CuAl$_2$-type). Furthermore the crystal structure of Ti$_5$Sb$_8$ was resolved from X-ray single crystal data to be isotypic to Zr$_{2.6}$Ti$_{2.4}$Sb$_8$-type. Narrow homogeneity regions (below 0.3 at %) were determined for all compounds with the exception for Ti$_3$Sb (from 21.9 to 24.4 at. % Sb), Ti$_{11-x}$Sb$_{8-y}$ (from 41.9 to 43.0 at. % Sb) and TiSb (from 49.5 to 50 at. %). Temperature stability ranges were derived by DTA for all compounds except for Ti$_5$Sb$_3$, which melts congruently above 1600 °C. ZrSb$_2$ (TiAs$_2$-structure type) melts incongruently ℓ + Zr$_{11}$Sb$_{18}$ = ZrSb$_2$ at 1363 °C. Isostructural HfSb$_2$ decomposes in an invariant peritectic reaction ℓ + Hf$_5$Sb$_9$ ↔ HfSb$_2$ at 980 °C. Binary Hf$_5$Sb$_9$, known as high temperature "β-HfSb$_2$″, exists in the narrow temperature range from 1277 °C (ℓ + HfSb ↔ Hf$_5$Sb$_9$) and 775 ± 25 °C (Hf$_5$Sb$_9$ ↔ HfSb + HfSb$_2$). The solubility of Zr and Hf in (Sb) in all samples investigated is below 0.2 at. %.

From single-phase samples MSb$_2$ (M = Ti, Zr, Hf) we elucidated a series of physical properties in detailed investigations of electrical

resistivity (from 4.2 K to 825 K), specific heat, thermal conductivity and thermal expansion behavior (from 4.2 K to 300 K), Seebeck coefficient (from 300 K to 825 K) and elastic moduli and hardness at room temperature.

It should be noted, that the thermal expansion coefficient of $TiSb_2$ is similar to the average values of Co-based *p*-type Sb-skutterudites, whilst the values of $ZrSb_2$ and $HfSb_2$ compounds are close to those for Co-based *n*-type Sb-skutterudites. It is furthermore comforting to learn, that thermal- and electrical conductivities of the MSb_2 compounds are significantly higher than those for highly efficient p- and n-type skutterudites and do not hamper electric and thermal heat flows in the contact zones.

Therefore the data collected throughout this work will serve to evaluate the potential of M_xSb_y compounds (M = Ti, Zr, Hf) for thermoelectric devices, where these phases predominantly may appear in the diffusion zones of hot metal electrodes with p- and n-type skutterudites and/or Sb-rich half Heusler alloys.

Acknowledgements

References

[1] J.L. Gomez-Camer, C. Villevieille, P. Novak, Antimony based negative electrodes for next generation Li-ion batteries, J. Mater. Chem. A 1 (2013) 13011–13016.

[2] J.L. Gomez-Camer, P. Novak, Polyacrylate bound $TiSb_2$ electrodes for Li-ion batteries, J. Power Sources 273 (2015) 174–179.

[3] V. Kordan, O. Zelinska, V. Pavlyuk, I. Oshchapovsky, R. Serkiz, Electrochemical lithiation of Ti_5M_3, Ti_3M and Zr_3M (M = Sn, Sb) binary intermetallics, Chem. Met. Alloys 9 (2016) 84–91.

[4] K.V.S. Rama, Superconductivity of hydrides Ti_3SbH_x, Phys. Lett. 93 (9) (1983) 492–494.

[5] A.V. Skripov, M.Y. Belyaev, S.A. Petrova, Hydrogen in the A15-type compound Ti_3Sb; NMR evidence for low-frequency localized motion of H atoms, J. Phys. Condens. Matter 4 (1992) L537–L542.

[6] H. Wu, A.V. Skripov, T.J. Udovic, J.J. Rush, S. Derakhshan, H. Kleinke, Hydrogen in Ti_3Sb and Ti_2Sb: neutron vibrational spectroscopy and neutron diffraction studies, J. Alloy. Comp 496 (2010) 1–6.

[7] G. Rogl, A. Grytsiv, P. Rogl, E. Bauer, M.B. Kerber, M. Zehetbauer, S. Puchegger, Multifilled nanocrystalline p-type didymium-skutterudites with ZT > 1.2, Intermetallics 18 (2010) 2435–2444.

[8] G. Rogl, A. Grytsiv, N. Melnychenko-Koblyuk, E. Bauer, S. Laumann, P. Rogl, Compositional dependence of the thermoelectric properties of $(Sr_xBa_xYb_{1−2x})_yCo_4Sb_{12}$ skutterudites, J. Phys. Condens. Matter 23 (2011) 1–11 27560.

[9] G. Schierning, R. Chavez, R. Schmechel, B. Balke, G. Rogl, P. Rogl, Concepts for medium-high to high temperature thermoelectric heat-to-electricity conversion: a review of selected materials and basic considerations of module design, Transl. Mater. Res. 2 (2015) 1–26 025001.

[10] J. Fan, L. Chen, S. Bai, X. Shi, Joining of Mo to $CoSb_3$ by spark plasma sintering by inserting a Ti interlayer, Mater. Lett 58 (2004) 3876–3878.

[11] D. Zhao, H. Geng, L. Chen, Microstructure contact studies for skutterudite thermoelectric devices, Int. J. Appl. Ceram. Technol. 9 (4) (2012) 733–741.

[12] D. Zhao, H. Geng, X. Teng, Fabrication and reliability evaluation of $CoSb_3$/W-Cu thermoelectric element, J. Alloy. Comp. 517 (2012) 198–203.

[13] M. Armbrüster, Bindungsmodelle für intermetallische Verbindungen mit der Struktur des $CuAl_2$-Typs, PhD thesis University of Dresden, Germany, 2004.

[14] M. Armbrüster, R. Cardoso Gil, U. Burkhardt, Y. Grin, Refinement of the crystal structures of titanium diantimonide, $TiSb_2$, and vanadium diantimonide, $V_{0.96}Sb_2$, Z. Kristallogr. NCS 219 (3) (2004) 209–210.

[15] M. Armbrüster, W. Schnelle, U. Schwarz, Y. Grin, Chemical bonding in $TiSb_2$ and VSb_2; A quantum chemical and experimental study, Inorg. Chem. 46 (16) (2007) 6319–6328.

[16] E. Garcia, J.D. Corbett, Study of the crystal structures of ZrSb and β-$ZrSb_2$ and of the bonding in the two $ZrSb_2$ structures, J. Solid State Chem. 73 (1988) 452–467.

[17] F. Hulliger, $TiAs_2$-type phases, Nature 5 (1964) 991.

[18] H. Nowotny, J. Pesl, Untersuchungen in system titan-antimon, Monatsh. Chem. 82 (1951) 336–343 (in German).

[19] E. Garcia, J.D. Corbett, A synthetic and structural study of the zirconium-antimony system, J. Solid State Chem. 73 (1988) 440–451.

[20] N. Soheilnia, A. Assoud, H. Kleinke, $MA_8Sb_{2.8}$ (M = Zr, Hf; A = Si, Ge) A new series of ternary antimonides and not β-$ZrSb_2$, Inorg. Chem. 42 (22) (2003) 7319–7325.

[21] K. Schubert, K. Frank, R. Gohle, A. Maldonado, H.G. Meissner, Raman, Einige Strukturdaten mMetallischer Phasen (8), Naturwissenschaften 50 (1963) 41 (in German).

[22] A. Assoud, K.M. Kleinke, N. Soheilnia, H. Kleinke, T-Shaped nets of antimony atoms in the binary antimonide Hf_5Sb_9, Angew. Chem. Int. Ed. 43 (39) (2003) 5260–5262.

[23] H. Nowotny, R. Funk, J. Pesl, Kristallchemische Untersuchungen in den Systemen Mn-As, V-Sb, Ti-Sb, Monatsh. Chem. 82 (3) (1951) 513–525 (in German).

[24] H. Auer von Welsbach, H. Nowotny, A. Kohl, Untersuchung reibungspyrophorer Ti-Legierungen; Ti_2Bi, ein neuer Strukturtyp, Monatsh. Chem. 89 (1) (1958) 154–159 (in German).

[25] A. Kjekshus, F. Grønvold, J. Thorbjørnsen, On the phase relationships in the titanium-antimony system. The crystal structures of Ti_3Sb, Acta Chem. Scand. 16 (1962) 1493–1510.

[26] H. Kleinke, $Ti_5Si_{1.3}Sb_{1.7}$ the first titanium silicide antimonide, forming a crystal structure not found in either binary system, Can. J. Chem. 79 (2001) 1338–1343.

[27] A.Y. Kozlov, V.V. Pavlyuk, New ternary antimonides Ti_5XSb_2 with W_5Si_3 structure type, Intermetallics 11 (2003) 237–239.

[28] R. Berger, Crystallographic data on new arsenides and antimonides of titanium and scandium, Acta Chem. Scand. Ser. A 31 (6) (1977) 514–516.

[29] R. Berger, Structure refinement of Ti_5Sb_3 from single-crystal data, Acta Chem. Scand., Ser. A 31 (1977) 889–890.

[30] J. Steinmetz, B. Malaman, B. Roques, Structural study of vanadium antimonide (V_3Sb_2) and titanium antimonide (Ti_5Sb_3), Compt. R. Hebd. Seances Acad. Sci., Ser. C: Sci. Child. 284 (1977) 499–502 (in French).

[31] J.L. Murray, Phase Diagrams of Binary Titanium Alloys, ASM International, Metals Park, Ohio, 1987, pp. 282–284.

[32] Binary alloy phase diagrams, second ed., in: T.B. Massalski (Ed.), Materials Information Soc, vol. 3, Materials Park, Ohio, 1990.

[33] Pauling File Binaries Editions, Version 1.0, Release 2002/1, ASM International Materials Park, OH 44073–0002 USA.

[34] L.D. Dudkin, V.I. Vaidanich, The nature of the electrical conductivity of certain compounds of transition metals with $CuAl_2$-type lattices, Fiz. Tverd. Tela 2 (29) (1960) 404–405 in Russian; TR: Soviet Phys. Solid Stat. 2(1960) 377–378.

[35] S. Bobev, H. Kleinke, Instabilities in the linear Sb atom chain of the new binary antimonide $Ti_{11−x}Sb_{8−y}$, Chem. Mater. 15 (18) (2003) 3523–3529.

[36] H. Kleinke, A three-dimensional extended Sb network in the metallic antimonides $(M',Ti)_5Sb_8$ (M' = Zr, Hf, Nb, Mo), Inorg. Chem. 40 (2001) 95–100.

[37] Y. Zhu, H. Kleinke, The new binary antimonide Ti_5Sb_8, Z. Anorg. Allg. Chem. 628 (2002) 2233.

[38] H. Bie, S.H.D. Moore, D.G. Piercey, A.V. Tkachuk, O.Y. Zelinska, A. Mar, Ternary rare-earth titanium antimonides: phase equilibria in the RE–Ti–Sb (RE = La, Er) systems and crystal structures of $RE_2Ti_7Sb_{12}$ (RE = La, Ce, Pr, Nd) and $RETi_3(Sn_xSb_{1−x})_4$ (RE = Nd, Sm), J. Solid State Chem. 180 (2007) 2216–2224.

[39] S. Derakhshan, A. Assoud, K.M. Kleinke, E. Dashjav, X. Qiu, S.J.L. Billinge, H. Kleinke, Planar nets of Ti atoms comprising squares and rhombs in the new binary antimonide Ti_2Sb, J. Am. Chem. Soc. 126 (2004) 8295–8302.

[40] J.W. Kaiser, M.G. Haase, W. Jeitschko, A variety of different occupancies in isotypic compounds: ternary antimonides and bismuthides with the ideal formulas $T_5T'Sb_3$ and $T_5T'Bi_3$ (T = Ti, Zr, Hf; T' = late transition metals) and the binary antimonide $Ti_{4.80}Sb_{3.29}$, all crystallizing with "filled" Mn_5Si_3 (Hf_5CuSn_3) type structure and structure refinement of $Ti_5Sb_{2.85}$ with β-Yb_5Sb_3 type structure, Z. Anorg. Allg. Chem. 627 (2001) 2369–2376.

[41] F. Failamani, P. Broz, D. Maccio, S. Puchegger, H. Müller, L. Salamakha, H. Michor, A. Grytsiv, A. Saccone, E. Bauer, G. Giester, P. Rogl, Constitution of the systems {V,Nb,Ta}-Sb and physical properties of diantimonides {V,Nb,Ta}Sb_2, Intermetallics 65 (2015) 94–110.

[42] W. Wacha, An integrated software system for x-ray-powder analysis, Institute of Solid State Physics, Vienna University of Technology, 1989 (In German), Diploma thesis.

[43] J. Rodriguez-Carvajal, Powder Diffraction, Satellite Meeting of the 15th Congress of IUCr, (1990), p. 127. Toulouse, France.

[44] J. Rodriguez-Carvajal, Recent advances in magnetic structure determination by neutron powder diffraction, Phys. B Condens. Matter 192 (1993) 55–69.

[45] G.M. Sheldrick, A short history of SHELX, Acta Crystallogr. A. 64 (1) (2007) 112–122.

[46] P. McArdle, Oscail, a program package for small-molecule single-crystal crystallography with crystal morphology prediction and molecular modelling, J. Appl. Cryst 50 (2017) 320–326.

[47] R. Lackner, The Effect of Substitution and Doping on the Thermoelectric Properties of $CePd_3$, (2007) PhD Thesis University of Technology Vienna, Austria.

[48] F. Röhrbacher, Transport and thermoelectric performance of Ba_8-based clathrates, Master thesis University of Technology Vienna, Austria, 2007.

[49] M. Rotter, H. Müller, E. Gratz, M. Doerr, M. Loewenhaupt, A miniature capacitance dilatometer for thermal expansion and magnetostriction, Rev. Sci. Instrum 69 (7) (1998) 2742–2746.

[50] M. Hansen, K. Anderko, Constitution of Binary Alloys, second ed., McGraw-Hill, New York, 1958.

[51] I. Elder, C.S. Lee, H. Kleinke, $Zr_{11}Sb_{18}$: a new binary antimonide exhibiting an unusual Sb atom, Inorg. Chem. 41 (2002) 538–545.

[52] J. Xu, K.M. Kleinke, H. Kleinke, Electronic structure and physical properties of Hf$_5$Sb$_9$ containing a unique T net of Sb atoms, Z. Anorg. Allg. Chem. 634 (2008) 2367–2372.

[53] D.M. Rowe, Handbook of Thermoelectrics, CRC Press, Boca Raton, FL, 2006.

[54] J. Callaway, Model for lattice thermal conductivity at low temperatures, Phys. Rev. 113 (1959) 1046–1051.

[55] J. Callaway, H.C. von Baeyer, Effect of point imperfections on lattice thermal conductivity, Phys. Rev. 120 (1960) 1149–1154.

[56] T.M. Tritt, Thermal conductivity: Theory, Properties and Applications, Clemson University, 2004.

[57] G. Rogl, P. Rogl, Mechanical properties of skutterudites, Sci. Adv. Mater. 3 (2011) 517–538.

[58] G.D. Mukherjee, C. Bansal, A. Chatterjee, Thermal expansion study of ordered and disordered Fe$_3$Al: an effective approach for the determination of vibrational entropy, Phys. Rev. Lett. 76 (11) (1996) 1876–1879.

[59] A. Junod, J. Muller, H. Rietschel, E. Schneider, Chaleur spécifique et transformation martensitique dans le système Nb$_{1-x}$Sn$_x$, J. Phys. Chem. Solids 39 (1978) 317–328 (in French).

[60] A. Junod, T. Jarlborg, J. Muller, Heat-capacity analysis of a large number of A15-type compounds, Phys. Rev. B 27 (1983) 1568–1585.

[61] C. Kittel, Introduction to Solid State Physics, eighth ed., John Wiley and Sons, 2004.

[62] G. Rogl, A. Grytsiv, M. Gürth, A. Tavassoli, C. Ebner, A. Wünschek, S. Puchegger, V. Soprunyuk, W. Schranz, E. Bauer, H. Müller, M. Zehetbauer, P. Rogl, Mechanical properties of half-Heusler alloys, Acta Mater. 107 (2016) 178–195.

[63] S.F. Pugh, Relations between the elastic moduli and the plastic properties of polycrystalline pure metals, Phil. Mag. 45 (1954) 823–843.

[64] O.L. Anderson, A simple method for calculating the Debye temperature from elastic constants, J. Phys. Chem. Solid. 24 (1963) 909–917.

[65] J. Jang, G.M. Pharr, Influence of indenter angle on cracking in Si and Ge during nanoindentation, Acta Mater. 56 (2008) 4458–4469.

[66] A. Leonardi, F. Furgile, S. Syngellakis, R.J.K. Wood, Numerical analysis of brittle materials fractured by sharp indenters, Eng. Fract. Mech. 77 (2010) 264–276.

[67] A.V. Skripov, A.A. Podlesnyak, P. Fischer, Neutron diffraction study of the structure of the A15-type deuteride Ti$_3$SbD$_{2.6}$, J. Alloy. Comp. 210 (1994) 27–29.

[68] B.T. Matthias, V.B. Compton, E. Corenzwit, Some new superconducting compounds, J. Phys. Chem. Solid. 19 (1–2) (1961) 130–133.

[69] A. Junod, F. Heiniger, J. Muller, Supraconductivité et chaleur spécifique d'alliages basés sur Ti$_3$Sb, Helv. Phys. Acta 43 (1970) 59–66.

[70] S. Ramakrishnan, G. Chandra, Normal state resistivity and Tc studies of superconducting Ti$_{1-x}$Sb$_x$ system, Phys. Lett. A 100 (1984) 441–444.

[71] S. Ramakrishnan, A.K. Nigam, G. Chandra, Susceptibility and upper critical field studies on A15 superconducting Ti$_3$Sb compound, Solid State Commun. 52 (1984) 641–643.

[72] A. Tkachuk, Y.K. Gorelenko, Y.V. Stadnyk, B.V. Padlyak, A. Jankowska-Frydel, O.I. Bodak, V. Sechovsky, Interaction between components in the Ti-Mn-Sb system at 870 K and the physical properties of Ti$_5$Mn$_{0.45}$Sb$_{2.25}$, J. Alloys Compd. 319 (2001) 74–79.

[73] A.Y. Kozlov, V.V. Pavlyuk, Investigation of the interaction between the components in the Ti-(Si,Ge)-Sb systems at 670 K, J. Alloy. Comp. 367 (2004) 76–79.

[74] H. Kleinke, Ti$_5$Sb$_{2.2}$Se$_{0.8}$: the first titanium antimonide selenide, J. Alloy. Comp. 336 (2002) 132–137.

[75] G.A. Melnyk, W. Tremel, The titanium-iron-antimony ternary system and the crystal and electronic structure of the interstitial compound Ti$_5$FeSb$_2$, J. Alloy. Comp. 349 (2003) 164–171.

[76] J.D. Donaldson, A. Kjekshus, D.G. Nicholson, T. Rakke, Properties of TiSb$_2$ and VSb$_2$, J. Less-Common Met. 4 (1975) 255–263.

[77] E.E. Havinga, H. Damsma, P. Hokkeling, Compounds and pseudobinary alloys with the CuAl$_2$ (C16)-type structure I. Preparation and X-Ray results, J. Less-Common Met. 27 (1972) 169–186.

[78] E. Parthé, L. Gelato, B. Chabot, M. Penzo, K. Cenzual, R. Gladyshevskii, TYPIX Standardized Data and Crystal Chemical Characterization of Inorganic Structure Types, Springer, Berlin, 1994.

[79] A. Kjekshus, On the crystal structures of ZrSb$_2$ and α-HfSb$_2$, Acta Chem. Scand. 26 (1972) 1633–1639.

[80] L. Romaka, A. Tkachuk, Yu Stadnyk, V.V. Romaka, A. Horyn, R. Korzh, Peculiarity of component interaction in Zr–Mn–{Sn, Sb} ternary systems, J. Alloys Compd. 611 (2014) 401–409.

[81] V.V. Romaka, L. Romaka, P. Rogl, Y. Stadnyk, N. Melnychenko, R. Korzh, Z. Duriagina, A. Horyn, Peculiarities of thermoelectric half-Heusler phase formation in Zr–Co–Sb ternary system, J. Alloy. Comp. 585 (2014) 448–454.

[82] I. Tokaychuk, Y. Tokaychuk, R. Gladyshevskii, The ternary system Hf–Ga–Sb at 600 ºC, Chem. Met. Alloys 6 (2013) 75–80.